Raman heterodyne studies of velocity diffusion effects in radio-frequency-laser double resonance

Chr. Tamm, E. Buhr, and J. Mlynek
Institut für Quantenoptik, Universität Hannover, Welfengarten 1, 3000 Hannover 1, Federal Republic of Germany
(Received 3 February 1986)

We report new results on the effect of collisions on radio-frequency (rf) -laser double resonances in an atomic vapor under conditions of velocity-selective optical pumping. Our experiments are performed on Zeeman resonances in the $4f^6 6s^2\,{}^7F_1 - 4f^6 6s\,6p\,{}^7F_0$ transition in samarium vapor in the presence of rare-gas perturbers (He, Ne, Ar, Xe). The collisional relaxation of the rf-generated sublevel coherence is studied using Raman heterodyne detection; this recently introduced spectroscopic technique is capable of separately yielding signal contributions originating from optically resonant and off-resonant atoms. The corresponding measurements clearly reveal that velocity-changing collisions (VCC) can completely determine the characteristics of the rf-laser double-resonance signals. Our experimental findings on the linewidths and line shapes of the rf resonances are in satisfactory quantitative agreement with theoretical predictions that are based on a novel four-level density-matrix calculation; here a Keilson-Storer collision kernel is used to describe the velocity diffusion processes. The comparison of calculated and measured results also permits us to derive cross sections for VCC and depolarizing collisions; moreover, information on the spectrum of the velocity changes connected with alignment-preserving collisions can be obtained.

I. INTRODUCTION

The study of collision effects in laser spectroscopy is in general only possible by taking into account the collisional perturbations of both the atomic internal state and the atomic velocities.[1] In a Doppler-broadened optical transition, "velocity-changing collisions" (VCC) can easily change the Doppler shift of the active atoms with respect to the velocity-selective driving laser field while preserving the optical preparation of the internal atomic state; this fact has been shown to significantly modify the signals obtained in saturation and polarization spectroscopy,[2] and in photon-echo experiments.[3] As a result of such studies, it is now widely accepted for a variety of spectroscopic techniques that the consideration of VCC effects is crucial for the proper interpretation of experiments where collisions might play a role. Only very little information, however, exists on the influence of VCC on the line shapes of radio-frequency (rf) -laser double-resonance signals;[4] here a detailed knowledge on VCC is also desirable because double-resonance experiments are often performed in an atomic or molecular gas in a buffer-gas atmosphere, i.e., in the presence of foreign-gas perturbers. In the present work we report a systematic experimental and theoretical study on the role of velocity-changing collisions in a rf-optical double-resonance experiment under conditions of velocity-selective laser excitation.

Typically, the techniques of radio-frequency-optical double resonance rely on the resonant excitation of transitions between closely spaced sublevels by means of a radio-frequency (rf) field; the light field is used to create the nonequilibrium population of the sublevels ("optical pumping") that is required for rf excitation, and to detect the rf-induced changes in the optical properties of the sample. Since the obtained resolution of the substate energy splitting is neither limited by the Doppler broadening of the optical transition nor by broadband optical excitation, the initial development of rf-optical double resonance spectroscopy has been possible with the use of incoherent broadband light sources.[5] Here, the measured linewidths were frequently determined by the radiative lifetime of the sublevels or by the average time between two depolarizing collisions;[6] as a result of the incoherent optical excitation, the time rate of collisional velocity changes was insignificant.

The situation can change drastically, however, for the case of velocity-selective laser excitation: If the optical pumping process and the optical detection of the rf resonance are both reduced to one velocity subgroup of the Doppler-broadened atomic ensemble, the time between subsequent collisional velocity changes limits the time interval of experimental observation of the rf-driven atoms. Thus, the resulting rf resonance linewidths can be directly related to the time rate of VCC. In a recent experiment, it has in fact been shown that Zeeman coherence-preserving, velocity-changing collisions can determine the characteristics of rf-laser double-resonance signals;[4] here the clear isolation of the influence of VCC was possible by comparing the signal contributions of optically resonant and off-resonant atoms with the use of a coherent Raman heterodyne detection technique.[7]

The purpose of this paper is to relate a number of the details of Raman heterodyne detection of rf resonances in the gas phase. We especially analyze the potential and the limitations of this new detection scheme for the study of collision effects in double-resonance spectroscopy. For our experiment, we consider an inhomogeneously broadened, Zeeman-split $J=1 \rightarrow J'=0$ transition; this atomic model system allows for a detailed theoretical description and, most importantly, it can be realized experimentally. In particular, the effect of collisional ve-

locity diffusion on the rf resonance line shapes of the Raman heterodyne signals can be easily calculated thus permitting a direct comparison of experimental results and theoretical predictions. It will be shown that the rf resonance signals contain information on the rate constants for VCC and depolarizing collisions as well as on characteristic values for the collisional velocity changes. In principle, the knowledge of these parameters allows an insight in the mechanisms governing the collisional relaxation of Zeeman sublevels.[8,9]

This paper is organized as follows. In Sec. II we briefly introduce the basic features of our experimental technique. A theoretical description for the effects of collisions on the line shapes of the Raman heterodyne signals is given in Sec. III. In Sec. IV we describe our experiment and display the experimental results obtained for a $J=1\rightarrow J'=0$ transition in atomic Sm vapor and various rare-gas collision partners. In Sec. V an analysis of the measured data and the comparison with theoretical predictions is used to derive initial values for the relevant collisional parameters. A critical summary and outlook is given in Sec. VI.

II. PRINCIPLE OF EXPERIMENT

The schematic of our experimental arrangement and the basic coherent Raman process for the studied case of a Zeeman-split $J=1-J'=0$ transition are shown in Fig. 1. The laser field $\mathbf{E}_0$ of frequency ω_E is polarized parallel to a transverse static magnetic field $\mathbf{B}_0$ that lifts the ground-state Zeeman-level degeneracy. The field $\mathbf{E}_0$ only drives the optical π transition ($m-m'=0$); resonant optical absorption and isotropic spontaneous reemission thereby induce a transfer of the $m=0$ population to the $m=\pm 1$ levels for atoms of the optically resonant velocity subgroup. In the limit of slow ground-state relaxation, this velocity-selective optical pumping process efficiently produces an alignment in the $J=1$ manifold. A rf field of frequency ω_H whose $\mathbf{B}$ vector is polarized along the light beam axis now resonantly excites $|\Delta m|=1$ sublevel coherences; via a two-photon process, the simultaneous presence of the light field $\mathbf{E}_0$ gives rise to coherent, copropagating Raman sidebands $\mathbf{E}_\pm$ with frequencies $\omega_E\pm\omega_H$. The Stokes ($\mathbf{E}_-$) and anti-Stokes ($\mathbf{E}_+$) fields follow the selection rules of σ^- and σ^+ radiation, respectively. As a consequence, $\mathbf{E}_+$ and $\mathbf{E}_-$ are linearly polarized in a direction that is perpendicular to $\mathbf{B}_0$ and to the polarization of the driving light field $\mathbf{E}_0$. A polarization analyzer in front of the photodetector is used to project carrier and orthogonally polarized sidebands of the Raman signal field along a common direction; at the photodiode, the strong optical carrier finally serves as a local oscillator for heterodyne detection of the Raman sidebands. The corresponding rf beat signal of frequency $\omega_H=|\omega_E-(\omega_E\pm\omega_H)|$ is detected by a phase-sensitive, narrow-bandwidth rf lock-in amplifier.

The modulation structure of the resulting field $\mathbf{E}_D(t)$ in front of the photodetector deserves a special discussion. In general, the Raman signal field emerging from the sample cell consists of two components which can be characterized by a phase relationship between carrier and Raman sidebands corresponding to the cases of pure amplitude (AM) and frequency (FM) modulation (see Fig. 2). With the superposition of $\mathbf{E}_0$ and $\mathbf{E}_\pm$ by means of an analyzer, these AM and FM components lead to an amplitude and frequency modulation of the detector field $\mathbf{E}_D(t)$, respectively. The heterodyne beat signal of a phase-insensitive, square-law photodetector now is connected only with the AM component of the Raman signal field and it can therefore be termed "AM Raman heterodyne signal" (AM-RHS). The complementary detection mode that isolates the FM-RHS can be realized by introducing a constant additional phase shift of $\theta=\pi/2$ for $\mathbf{E}_0$ with respect to $\mathbf{E}_\pm$: Figure 2 shows that this converts the FM component of the Raman signal field into amplitude

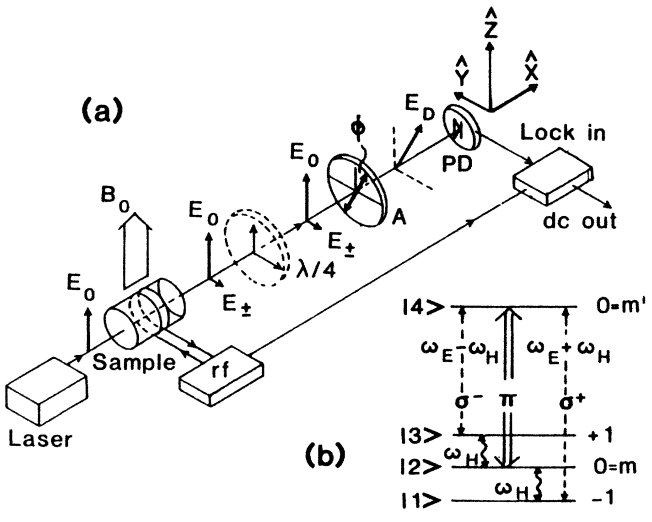

FIG. 1. (a) Experimental scheme. A, polarization analyzer; PD, photodetector; B_0, static magnetic field. The $\lambda/4$ plate is inserted with its main axes parallel to the polarization directions of $\mathbf{E}_0$ and $\mathbf{E}_\pm$ and is used only for the detection of the FM-RHS (see text). (b) Energy-level diagram for a Zeeman split $J=1-J'=0$ transition, showing the coherent Raman process.

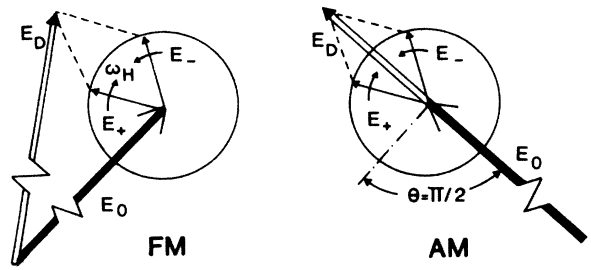

FIG. 2. Phase vectors of laser field $E_0(t)$ and frequency-shifted Raman sidebands $E_+(t),E_-(t)$ in a reference frame rotating with frequency ω_E for the cases of pure frequency (FM) and amplitude modulation (AM) of the superposition field $E_D(t)$. It can be seen that a constant phase shift of $\theta=\pi/2$ of E_0 with respect to E_+ and E_- converts FM to AM, and vice versa. If laser and Raman sideband fields have orthogonal polarization directions, this phase shift can be realized with a $\lambda/4$ plate (see text).

modulation, and vice versa. In our experiment, the required phase retardation in the Raman signal field can easily be obtained with a $\lambda/4$ plate in front of the analyzer as indicated in Fig. 1(a).

The separate study and comparison of AM- and FM-RHS is essential for the analysis of collision effects in our double-resonance experiment. To illuminate this point, we see in Fig. 3(a) an outline of the expected velocity distribution of rf-excited atoms; in the presence of collisions, the shape of this distribution is determined by the collisional redistribution of atomic velocities during the velocity-selective optical pumping and rf excitation processes. It can be seen from Figs. 3(a) and 3(b) that the AM-RHS is in our case sensitive only to optically resonant atoms whose Doppler shift with respect to the laser field is smaller than the homogeneous optical linewidth. Here, the optical pumping *and* the detection of the rf-excited sublevel coherence are equally reduced to one small velocity subgroup of the atomic ensemble. In contrast to this, the dispersive shape of the FM-RHS detection sensitivity shown in Fig. 3(c) implies that the contributions of optically resonant atoms are nearly completely canceled out in the observation of a velocity average. The detected FM-RHS therefore mainly arises from the asymmetry of the optically off-resonant wings of the distribution shown in Fig. 3(a); for an optical excitation of atoms with nonzero velocities, this asymmetry is due to rf-excited atoms that are partially thermalized by VCC.

It follows that collisions will affect the rf resonance linewidths of AM- and FM-RHS in a different manner:

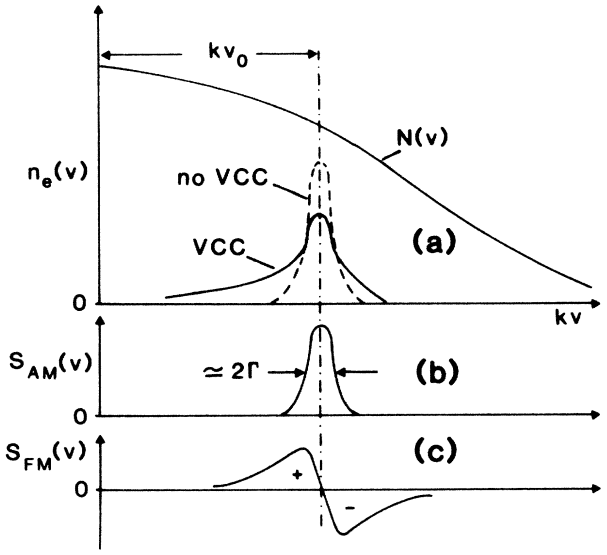

FIG. 3. (a) Outline of the velocity distribution of rf excited atoms $n_e(v)$ under conditions of velocity-selective optical pumping, showing the case of a partial thermalization of $n_e(v)$ due to VCC. It is assumed that the laser is tuned to the high-frequency wing ($kv_0 > 0$) of the thermal velocity distribution $N(v)$. (b), (c) Velocity-dependent detection sensitivities $S_{AM}(v)$ and $S_{FM}(v)$ of AM and FM Raman heterodyne detection. Γ denotes the homogeneous optical linewidth (HWHM). The measured Raman heterodyne signals are proportional to the velocity-integrated products $S_{AM}(v)n_e(v)$ and $S_{FM}(v)n_e(v)$, respectively.

The AM-RHS linewidth depends on the average time interval between two collisions that either depolarize or lead to velocity changes being sufficiently strong to take the active atoms in and out of optical resonance. In contrast, the linewidth of the FM-RHS can be expected to be determined by the time constants of collisional depolarization and of velocity thermalization. The comparison of AM- and FM-RHS thus allows one to study the influence of collisional velocity diffusion on optically detected rf resonance line shapes. In turn, the measured AM- and FM-RHS linewidths can be used to obtain quantitative information on both depolarizing and sublevel coherence-preserving, velocity-changing collisions.

III. THEORY

In this section AM- and FM-RHS are calculated with the use of a density-matrix formalism that describes the time evolution of the atomic ensemble in the presence of a laser field and a magnetic rf field. In a perturbative treatment, the corresponding equations of motion are solved under steady-state conditions. Here, the effects of velocity-selective optical pumping and of collisions of the active atoms with foreign "perturber" atoms are taken into account with the explicit inclusion of the collisional velocity diffusion of optically pumped atoms. The resulting theoretical predictions for the influence of VCC on the rf resonance line shapes of AM- and FM-RHS are discussed.

A. Basic equations

The atomic vapor contained in the sample cell simultaneously interacts with an optical field of frequency ω_E,

$$\mathbf{E}_0(\mathbf{r},t) \equiv \frac{E_0}{2}\hat{\mathbf{e}}_z e^{i(\omega_E t - kx)} + \text{c.c.} , \tag{3.1}$$

and with a magnetic rf field of frequency ω_H,

$$\mathbf{B}_H(t) \equiv \frac{B_H}{2}\hat{\mathbf{e}}_x e^{i\omega_H t} + \text{c.c.} \tag{3.2}$$

In (3.1), we neglect the limited transverse dimensions of the experimental laser field. As a consequence, we will proceed without an *ab initio* calculation of, e.g., transit-time effects or signal features that can result from the propagation of laser and Raman sideband fields with finite beam diameters.[10]

The spatial phase variation of the magnetic rf field is ignored in (3.2) because its wavelength is assumed to be much larger than the optical wavelength and the length L of the optical interaction region:

$$\omega_H \ll \omega_E, \quad \omega_H \ll \frac{2\pi c}{L} . \tag{3.3}$$

The atomic Hamiltonian $\mathscr{H}$ is assumed to include the atom-field interaction semiclassically in the dipole approximation,

$$\mathscr{H} = \mathscr{H}_0 + \mathscr{H}_I , \tag{3.4a}$$

$$\mathscr{H}_I = -\boldsymbol{\mu}_E \cdot \mathbf{E}_0(\mathbf{r},t) - \boldsymbol{\mu}_H \cdot \mathbf{B}_H(t) , \tag{3.4b}$$

where $\boldsymbol{\mu}_E$ and $\boldsymbol{\mu}_H$ are the electric and magnetic dipole

moment operators, respectively. In the basis of eigenstates $|i\rangle$ as given in Fig. 1(b), the nonvanishing matrix elements $H_{ij}=\langle i|\mathscr{H}|j\rangle$ are easily calculated. With g_J denoting Landé's factor and with μ_B defining Bohr's magneton, the matrix elements can be written in the form

$$H_{44}=\hbar\Omega_E \ , \tag{3.5a}$$

$$H_{33}=-H_{11}=g_J\mu_B B_0=\hbar\Omega_H \ , \tag{3.5b}$$

$$H_{24}=-\hbar\beta_E e^{i(\omega_E t-kx)}+\text{c.c.} \ , \tag{3.5c}$$

$$H_{12}=H_{23}=-\hbar\beta_H e^{i\omega_H t}+\text{c.c.} \ , \tag{3.5d}$$

with the optical and magnetic dipole coupling strengths

$$\beta_E\equiv\frac{E_0}{2\hbar}\mu_{24}\equiv\frac{E_0}{2\hbar}\langle 2|\boldsymbol{\mu}_E\cdot\hat{\mathbf{e}}_z|4\rangle \ , \tag{3.6a}$$

$$\beta_H\equiv\frac{B_H}{2\hbar}\mu_{12}\equiv\frac{B_H}{2\hbar}\langle 1|\boldsymbol{\mu}_H\cdot\hat{\mathbf{e}}_x|2\rangle \ . \tag{3.6b}$$

For the further calculations, we will use a representation of wave functions[11] that yields the following dipole matrix elements:

$$\mu_{24}=\mu_{42}\equiv\mu_E \ , \tag{3.7a}$$

$$\mu_{14}=\mu_{34}\equiv\langle 1|\boldsymbol{\mu}_E\cdot\hat{\mathbf{e}}_y|4\rangle\equiv-\frac{i}{\sqrt{2}}\mu_E \ , \tag{3.7b}$$

$$\mu_{12}=\mu_{21}=\mu_{23}=\mu_{32}\equiv\mu_H \ . \tag{3.7c}$$

1. Density-matrix formalism

If radiation-induced changes of the atomic velocities and collective effects such as radiation trapping are neglected, the density-matrix equations of motion for an atomic ensemble moving with velocity $\mathbf{v}$ are given by[12]

$$\frac{\partial\rho(\mathbf{r},\mathbf{v},t)}{\partial t}+\mathbf{v}\cdot\nabla\rho(\mathbf{r},\mathbf{v},t)=-\frac{i}{\hbar}[\mathscr{H}(\mathbf{r},t),\rho(\mathbf{r},\mathbf{v},t)]+\{\cdots\} \ . \tag{3.8}$$

The curly brackets on the right-hand side of (3.8) represent the phenomenological addition of relaxation and transport terms that will be carried out below. A solution of (3.8) is facilitated if the nondiagonal density-matrix elements ρ_{12},ρ_{23} ("Hertzian" coherence[13]) and $\rho_{14},\rho_{24},\rho_{34}$ ("optical" coherence) are written in the field-interaction representation ($v\equiv\mathbf{v}\cdot\hat{\mathbf{e}}_x$):

$$\rho_{12}(\mathbf{r},\mathbf{v},t)=\tilde{\rho}_{12}(v)e^{i\omega_H t} \ , \tag{3.9a}$$

$$\rho_{23}(\mathbf{r},\mathbf{v},t)=\tilde{\rho}_{23}(v)e^{i\omega_H t} \ , \tag{3.9b}$$

and

$$\rho_{14}(\mathbf{r},\mathbf{v},t)=\tilde{\rho}_{14}(v)e^{i[(\omega_E+\omega_H)t-kx]} \ , \tag{3.9c}$$

$$\rho_{24}(\mathbf{r},\mathbf{v},t)=\tilde{\rho}_{24}(v)e^{i(\omega_E t-kx)} \ , \tag{3.9d}$$

$$\rho_{34}(\mathbf{r},\mathbf{v},t)=\tilde{\rho}_{34}(v)e^{i[(\omega_E-\omega_H)t-kx]} \ . \tag{3.9e}$$

The $\Delta m=2$ sublevel coherence ρ_{13} will not be considered here since it is important only for the calculation of rf saturation effects.[5] Within the rotating-wave approximation (RWA), which neglects nonresonant terms, the stationary solutions of (3.8) are now characterized by

$$\frac{\partial\rho_{ii}(v)}{\partial t}=0, \quad \frac{\partial\tilde{\rho}_{ij}(v)}{\partial t}=0 \ \ (i\neq j) \ . \tag{3.10}$$

In the case of a thermal velocity distribution, the calculated macroscopic density-matrix elements are normalized through the condition

$$\sum_{i=1}^{4}\langle\rho_{ii}(v)\rangle\equiv\int N(v)dv\equiv N \ , \tag{3.11}$$

where $\langle\ \rangle$ denotes the velocity integration, N the number density, and $N(v)$ the one-dimensional Maxwell-Boltzmann distribution

$$N(v)=\frac{N}{\sqrt{\pi}u}\exp\left[-\left[\frac{v}{u}\right]^2\right] \ . \tag{3.12}$$

Here $u=(2k_BT/m_A)^{1/2}$ denotes the most probable thermal speed being determined by Boltzmann's constant k_B, absolute temperature T, and mass of active atoms m_A.

2. Calculation of Raman heterodyne signals

Let us now consider the generation of the Raman sidebands $E_\pm$ and the heterodyne detection of the corresponding AM and FM components of the Raman signal field. The frequency-shifted Raman polarization is of the form

$$\mathbf{P}_\pm(\mathbf{r},t)=\hat{\mathbf{e}}_y\tfrac{1}{2}(P_+e^{i[(\omega_E+\omega_H)t-kx]}+P_-e^{i[(\omega_E-\omega_H)t-kx]})+\text{c.c.} \ , \tag{3.13}$$

and it is related to the optical coherence amplitudes $\tilde{\rho}_{14}$ and $\tilde{\rho}_{34}$ by

$$P_+=i\sqrt{2}\mu_E\langle\tilde{\rho}_{14}\rangle \ , \tag{3.14a}$$

$$P_-=i\sqrt{2}\mu_E\langle\tilde{\rho}_{34}\rangle \ . \tag{3.14b}$$

This polarization acts as a source term in Maxwell's wave equation. For an optically thin sample, with the conditions of (3.3), and in the limit of slowly varying field envelopes, the amplitudes of the Raman sidebands are given by

$$E_+=-i\frac{kL}{2\epsilon_0}P_+=\frac{kL}{\epsilon_0}\frac{\mu_E}{\sqrt{2}}\langle\tilde{\rho}_{14}\rangle \ , \tag{3.15a}$$

$$E_-=-i\frac{kL}{2\epsilon_0}P_-=\frac{kL}{\epsilon_0}\frac{\mu_E}{\sqrt{2}}\langle\tilde{\rho}_{34}\rangle \ . \tag{3.15b}$$

The resulting Raman sideband field $\mathbf{E}_\pm(r,t)$ is copropagating with the orthogonally polarized laser field (3.4). It has the form

$$\mathbf{E}_{\pm}(\mathbf{r},t)=\hat{\mathbf{e}}_y\tfrac{1}{2}(E_+e^{i[(\omega_E+\omega_H)t-kx]}+E_-e^{i[(\omega_E-\omega_H)t-kx]})+\text{c.c.} \tag{3.16}$$

For the experimental setup shown in Fig. 1(a), the total resulting field in front of the photodetector $\mathbf{E}_D(t)$ can now be calculated. We describe the action of retardation plate and analyzer with the use of a Jones-Matrix formalism[14] and obtain

$$\mathbf{E}_D(t)\equiv\begin{bmatrix}\mathbf{E}_D(t)\hat{\mathbf{e}}_z\\ \mathbf{E}_D(t)\hat{\mathbf{e}}_y\end{bmatrix}=\frac{1}{2}\begin{bmatrix}\cos^2\phi & \sin\phi\cos\phi\\ \sin\phi\cos\phi & \sin^2\phi\end{bmatrix}\begin{bmatrix}1 & 0\\ 0 & e^{i\theta}\end{bmatrix}\begin{bmatrix}E_0\\ E_+e^{i\omega_H t}+E_-e^{-i\omega_H t}\end{bmatrix}e^{i\omega_E t}+\text{c.c.} \tag{3.17}$$

With (3.17), we take into account that the orthogonally polarized laser and Raman sideband fields can be mutually phase shifted by an angle θ through the retardation plate and that they are then projected in a common direction by an analyzer inserted under an angle ϕ to allow for interference. To consider the role of the retardation plate in our detection scheme, we now first discuss the case $\theta=0$ (no phase retardation).

$\theta=0$: In this case, (3.17) can be reduced to the form

$$\mathbf{E}_D(t)=\tfrac{1}{2}\cos\phi(\hat{\mathbf{e}}_z\cos\phi+\hat{\mathbf{e}}_y\sin\phi)E_0\left[1+\frac{\sin\phi}{\cos\phi}[\mathrm{Re}(m_{\mathrm{AM}}e^{-i\omega_H t})+i\,\mathrm{Re}(m_{\mathrm{FM}}e^{-i\omega_H t})]\right]e^{i\omega_E t}+\text{c.c.} \tag{3.18}$$

The modulation parameters m_{AM} and m_{FM} here describe a corresponding amplitude and frequency modulation of the detector field $\mathbf{E}_D(t)$ with frequency ω_H ($m_{\mathrm{AM}},m_{\mathrm{FM}}\ll 1$). With the use of (3.15), m_{AM} and m_{FM} can directly be related to different linear combinations of density-matrix elements:

$$m_{\mathrm{AM}}=\frac{kL}{\epsilon_0}\frac{\mu_E}{\sqrt{2}}\frac{\langle\tilde{\rho}_{41}\rangle+\langle\tilde{\rho}_{34}\rangle}{2E_0}, \tag{3.19a}$$

$$m_{\mathrm{FM}}=\frac{kL}{\epsilon_0}\frac{\mu_E}{\sqrt{2}}i\frac{\langle\tilde{\rho}_{41}\rangle-\langle\tilde{\rho}_{34}\rangle}{2E_0}. \tag{3.19b}$$

We note that for $\theta=0$, the heterodyne beat signal of a square-law photodetector is connected only with m_{AM} (AM-RHS) since the detector is not sensitive to the optical phase.

$\theta\neq 0$: For nonzero values of θ, the FM-RHS connected with m_{FM} can also be monitored. In this case, the heterodyne beat signal derived from (3.17) is of the form[4]

$$|E_D|^2_{\mathrm{beat}}=2E_0\sin\phi\cos\phi\{E_0\cos\theta[\mathrm{Re}(m_{\mathrm{AM}})\cos(\omega_H t)+\mathrm{Im}(m_{\mathrm{AM}})\sin(\omega_H t)]-E_0\sin\theta[\mathrm{Re}(m_{\mathrm{FM}})\cos(\omega_H t)+\mathrm{Im}(m_{\mathrm{FM}})\sin(\omega_H t)]\}. \tag{3.20}$$

It can be seen that for $\theta=(2n+1)\pi/2$ ($n=1,2,3,\ldots$), the detector signal is determined only by m_{FM}. As a consequence, the FM-RHS can be isolated by inserting a $\lambda/4$ plate in front of the analyzer as indicated in Fig. 1(a).

Equation (3.20) also shows that AM and FM rf beat signals can contain in-phase [$\cos(\omega_H t)$] and quadrature [$\sin(\omega_H t)$] components with respect to the driving rf field. They are related to the real and imaginary parts of the modulation parameters, respectively. According to (3.19), the phase-sensitive detection of AM- and FM-RHS thus can yield the complete information on the atomic time evolution as contained in the complex optical coherence amplitudes $\tilde{\rho}_{14}$ and $\tilde{\rho}_{34}$.

B. Calculation of rf resonance line shapes

The calculation of the rf resonance line shapes of AM- and FM-RHS requires a solution of (3.8). The characteristics of this solution are in turn determined by the structure of the relaxation terms of (3.8), which will be specified now to describe the effects of spontaneous emission, thermal motion of the active atoms through the optical interaction region, and of collisions with perturber atoms.

In the treatment of collisional relaxation, we consider here the effect of both depolarizing collisions and VCC on the ground-state manifold. This can be done by introducing in (3.8) appropriate relaxation and transport terms that result in semiclassical transport equations[8] for ground-state population difference and Hertzian coherence. The velocity diffusion of the excited-state population density $\rho_{44}(v)$ is neglected since the lifetime of the optically excited state is assumed to be much shorter than the ground-state lifetime. Furthermore, we also neglect the diffractive contributions in the collisional scattering of the atomic optical dipoles, which in general is well justified in case of continuous wave (cw) optical excitation.[15] The collisional dephasing of the optical dipoles that leads to a pressure broadening of the homogeneous optical linewidth is taken into account by a corresponding damping constant for the macroscopic optical coherence.

1. Equations of motion in the presence of collisions

With the use of the rotating-wave approximation, simple steady-state density-matrix equations now can be derived from (3.8). We define the rf and optical tuning parameters by

$$\Delta_H \equiv \omega_H - \Omega_H \ , \tag{3.21a}$$

$$kv_0 \equiv \omega_E - \Omega_E \ , \tag{3.21b}$$

and obtain from (3.8) the following equations:

$$(kv_0 - kv - i\Gamma)\tilde{\rho}_{24}(v) = \beta_E[\rho_{44}(v) - \rho_{22}(v)] + \beta_H[\tilde{\rho}_{14}(v) + \tilde{\rho}_{34}(v)] \ , \tag{3.22a}$$

$$\Gamma_4 \rho_{44}(v) = i\beta_E[\tilde{\rho}_{24}(v) - \tilde{\rho}_{42}(v)] \ , \tag{3.22b}$$

$$(\gamma_g + \gamma_{VCC})\rho_{22}(v) = i\beta_E[\tilde{\rho}_{42}(v) - \tilde{\rho}_{24}(v)] + i\beta_H[\tilde{\rho}_{12}(v) - \tilde{\rho}_{21}(v) + \tilde{\rho}_{32}(v) - \tilde{\rho}_{23}(v)] + \frac{\Gamma_4}{3}\rho_{44}(v) + \frac{\gamma_g}{3}N(v) + \int W(v' \to v)\rho_{22}(v')dv' \ , \tag{3.22c}$$

$$(\gamma_g + \gamma_{VCC})\rho_{11}(v) = i\beta_H[\tilde{\rho}_{21}(v) - \tilde{\rho}_{12}(v)] + \frac{\Gamma_4}{3}\rho_{44}(v) + \frac{\gamma_g}{3}N(v) + \int W(v' \to v)\rho_{11}(v')dv' \ , \tag{3.22d}$$

$$(i\Delta_H + \gamma_g + \gamma_{VCC})\tilde{\rho}_{12}(v) = i\beta_H[\rho_{22}(v) - \rho_{11}(v)] - i\beta_E\tilde{\rho}_{14}(v) + \int W(v' \to v)\tilde{\rho}_{12}(v')dv' \ , \tag{3.22e}$$

$$(kv_0 - kv + \Delta_H - i\Gamma)\tilde{\rho}_{14}(v) = -\beta_E\tilde{\rho}_{12}(v) + \beta_H\tilde{\rho}_{24}(v) \ . \tag{3.22f}$$

The three remaining equations that determine $\rho_{33}(v)$, $\tilde{\rho}_{32}(v)$, and $\tilde{\rho}_{34}(v)$ are identical to Eqs. (3.22d–(3.22f) if Δ_H is replaced by $-\Delta_H$ in (3.22e) and (3.22f). This leads to the symmetry relations

$$\rho_{33}(v) = \rho_{11}(v) \ , \tag{3.23a}$$

$$\tilde{\rho}_{32}(v, \Delta_H) = \tilde{\rho}_{12}(v, -\Delta_H) \ , \tag{3.23b}$$

$$\tilde{\rho}_{34}(v, \Delta_H) = \tilde{\rho}_{14}(v, -\Delta_H) \ . \tag{3.23c}$$

In (3.22a)–(3.22f), Γ_4 is the rate of isotropic spontaneous decay for the population of the optically excited state, and $\Gamma = \Gamma_4/2 + \Gamma_c$ denotes the natural and collision-induced decay of optical coherence. The relaxation to thermal equilibrium of the ground-state sublevel population densities and of Hertzian coherence due to depolarizing collisions and thermal motion is described by the decay rate γ_g. The collisional velocity diffusion of the optically pumped, rf-driven atoms out of and into a given velocity subgroup is described through the terms containing the VCC rate constant γ_{VCC} and the collision kernel $W(v' \to v)$, respectively; here, γ_{VCC} gives the overall time rate of the collisions described by $W(v' \to v)$. All rate constants are assumed to be speed independent.

In Eqs. (3.22c)–(3.22e), the collision kernel $W(v' \to v)$ denotes the velocity-change spectrum connected with nondepolarizing collisions. This spectrum in general contains contributions of both collisional scattering along classical trajectories and of quantum-diffractive scattering. To give a picture for the physically expected shape of $W(v' \to v)$, we recall that for hard-sphere collisions, the classical large-angle scattering and the diffractive small-angle scattering both contribute about 50% to the total scattering cross section: The total hard-sphere velocity-change spectrum consists of a narrow diffractive peak of an approximate width of $|v - v'| \simeq 2\hbar/(m_A b)$ (b is the radius of the hard-sphere potential) and of a broad classical pedestal whose width can reach the width of the thermal velocity distribution of the active atoms.[15]

In the limit of a small anisotropy of the collision potential for both diffractive and classical collisions, a shape similar to the hard-sphere VCC spectrum can also be expected for the velocity-change spectrum connected with nondepolarizing collisions, $W(v' \to v)$. However, for the theoretical analysis of our experiment, we will neglect the diffractive enhancement of the small-angle contributions in $W(v' - v)$: This seems to be justified since for typical active atom-perturber systems, the effect of diffractive collisions in cw experiments can be expected to be rather small due to the natural linewidth-limited velocity resolution of such experiments.[15] Moreover, the effect even of a large number of diffractive velocity changes can be efficiently masked if the ground-state sublevel coherence is partially preserved in large-angle scattering events.

In the further calculation, $W(v' \to v)$ will be represented by the phenomenological Keilson-Storer collision kernel[16] that is of the simple analytical form

$$W(v' \to v) = \gamma_{VCC}[\pi(\Delta u)^2]^{-1/2} \exp\left[-\left[\frac{v - \alpha v'}{\Delta u}\right]^2\right] \ , \tag{3.24a}$$

$$\Delta u = (1 - \alpha^2)^{1/2} u, \quad 0 \le \alpha < 1 \ . \tag{3.24b}$$

The Keilson-Storer kernel can be used as a good approximation for the nondiffractive part of the hard-sphere collision kernel.[17] The kernel (3.24) corresponds to a Gaussian spectrum of velocity changes centered at $v - \alpha v' = 0$, with a width corresponding to a rms velocity change of $|v - v'| = \Delta u/\sqrt{2}$.

2. Perturbation solution

We can now perform a perturbation solution of (3.22) and (3.23) to calculate the optical coherence amplitudes

$\tilde{\rho}_{14}(v)$ and $\tilde{\rho}_{34}(v)$ that determine the Raman heterodyne signals. In analogy to nonlinear processes involving two optical fields, different "perturbation chains"[12] have to be taken into account also in the perturbative treatment of the considered rf-laser double resonance process. It can be shown, however, that in the limit of a strongly Doppler-broadened optical transition ($ku \gg \Gamma$) and of a long-lived ground state ($\gamma_g < \Gamma$), significant signal contributions only arise from the following perturbation chain:[18]

$$\rho_{22} \xrightarrow{\beta_E} \rho_{24} \xrightarrow{\beta_E} \begin{Bmatrix} \rho_{44} \\ \rho_{22}-\rho_{11} \\ \rho_{22}-\rho_{33} \end{Bmatrix} \xrightarrow{\beta_H} \begin{Bmatrix} \tilde{\rho}_{12} \\ \tilde{\rho}_{32} \end{Bmatrix} \xrightarrow{\beta_E} \begin{Bmatrix} \tilde{\rho}_{14} \\ \tilde{\rho}_{34} \end{Bmatrix} . \tag{3.25}$$

The excitation steps described by this chain can be easily interpreted as an optical pumping process that produces a ground-state population difference (longitudinal alignment) through resonant absorption and spontaneous reemission, an excitation of Hertzian coherence (oscillating transversal alignment) by the rf field, and a coherent Raman process that leads to the frequency-shifted coherent Raman emission driven by $\tilde{\rho}_{14}$ and $\tilde{\rho}_{34}$. We now calculate AM- and FM-RHS according to the formal way described by (3.25). From (3.22a) and (3.22b), it follows that the velocity-selective optical excitation leads to a population density $\rho_{44}(v)$ given by

$$\rho_{44}(v) = \frac{N(v)}{3} \frac{2\Gamma}{\Gamma_4} \frac{\beta_E^2}{(kv_0 - kv)^2 + \Gamma^2} . \tag{3.26}$$

For $\gamma_{VCC} = 0$ (no collisional velocity changes), the velocity distribution of the ground-state population difference $\rho_D(v) \equiv \rho_{11}(v) - \rho_{22}(v)$ is proportional to the one of $\rho_{44}(v)$. In the presence of VCC, however, the velocity distribution of optically pumped atoms $\rho_D(v)$ is also determined by velocity diffusion. From (3.22c) and (3.22d), we can derive a transport equation that describes the steady-state velocity distribution of $\rho_D(v)$:

$$(\gamma_g + \gamma_{VCC})\rho_D(v) = \Gamma_4 \rho_{44}(v) + \gamma_{VCC}[\pi(\Delta u)^2]^{-1/2} \int \exp\left[-\left[\frac{v - \alpha v'}{\Delta u} \right]^2 \right] \rho_D(v')dv' . \tag{3.27}$$

With $\beta_H \rho_D(v)$ as the source term, a similar expression is obtained from (3.22e) for the resonant excitation of Hertzian coherence:

$$(i\Delta_H + \gamma_g + \gamma_{VCC})\tilde{\rho}_{12}(v) = -i\beta_H \rho_D(v) + \gamma_{VCC}[\pi(\Delta u)^2]^{-1/2} \int \exp\left[-\left[\frac{v - \alpha v'}{\Delta u} \right]^2 \right] \rho_{12}(v')dv' . \tag{3.28}$$

We solve the above integral equations by iteration; adopting a formalism used in Ref. 12, the solutions of (3.27) and (3.28) can be written in the form

$$\rho_D(v) = \frac{\Gamma_4}{\gamma_g + \gamma_{VCC}} \int Q_D(v' \to v) \rho_{44}(v')dv' , \tag{3.29a}$$

$$\tilde{\rho}_{12}(v) = -\frac{i\beta_H}{i\Delta_4 + \gamma_g + \gamma_{VCC}} \int Q_{12}(v' \to v) \rho_D(v')dv' , \tag{3.29b}$$

with the propagators Q_D and Q_{12} given by

$$Q_D(v' \to v) = \delta(v - v') + \sum_{n=1}^{\infty} \left[\frac{\gamma_{VCC}}{\gamma_g + \gamma_{VCC}} \right]^n K_n(v, v') , \tag{3.30a}$$

$$Q_{12}(v' \to v) = \delta(v - v') + \sum_{n=1}^{\infty} \left[\frac{\gamma_{VCC}}{i\Delta_H + \gamma_g + \gamma_{VCC}} \right]^n K_n(v, v') , \tag{3.30b}$$

and

$$K_n(v, v') \equiv [\pi u^2 (1 - \alpha^{2n})]^{-1/2} \times \exp\left[-\frac{(v - \alpha^n v')^2}{u^2(1 - \alpha^{2n})} \right] . \tag{3.31}$$

To obtain analytical results for $\rho_D(v)$ and $\tilde{\rho}_{12}(v)$, we now make the approximation $k\Delta u \gg \Gamma$ for the width of the collision kernel $W(v' \to v)$. Since γ_{VCC} gives the total time rate of collisions described by $W(v' \to v)$, the limit $k\Delta u \gg \Gamma$ implies that γ_{VCC} denotes the time rate of collisions that remove the active atoms from optical resonance. We note that the approximation $k\Delta u \gg \Gamma$ is justified only if the contributions of diffractive collisions to the velocity-change spectrum can be neglected (see above). Some simple consequences that may arise for cases where the assumption $k\Delta \gg \Gamma$ is inadequate will be discussed later on. For $k\Delta u \gg \Gamma$, the integration of (3.29a) yields

$$\rho_D(v) = \frac{2}{3} \frac{\beta_E^2}{\gamma_g + \gamma_{VCC}} \left[\frac{\Gamma N(v)}{(kv_0 - kv)^2 + \Gamma^2} + \frac{\pi}{k} N(v_0) \sum_{n=1}^{\infty} \left[\frac{\gamma_{VCC}}{\gamma_g + \gamma_{VCC}} \right]^n K_n(v, v_0) \right] . \tag{3.32}$$

Correspondingly, with (3.29b) and (3.32), one obtains in a straightforward calculation the velocity distribution of the rf-excited sublevel coherence:[18]

$$\tilde{\rho}_{12}(v)=-\frac{2}{3}\frac{\beta_E^2}{\gamma_g+\gamma_{VCC}}\frac{i\beta_H}{i\Delta_H+\gamma_g+\gamma_{VCC}}\left[\frac{\Gamma N(v)}{(kv_0-kv)^2+\Gamma^2}+\frac{\pi}{k}N(v_0)\sum_{n=1}^{\infty}\left[\frac{\gamma_{VCC}}{\gamma_g+\gamma_{VCC}}\right]^n[1+P_n(\Delta_H)]K_n(v,v_0)\right] \tag{3.33}$$

with

$$P_n(\Delta_H)\equiv\frac{\gamma_g+\gamma_{VCC}}{i\Delta_H}\left[1-\left[\frac{\gamma_g+\gamma_{VCC}}{i\Delta_H+\gamma_g+\gamma_{VCC}}\right]^n\right], \quad \Delta_H\neq 0$$
$$P_n(\Delta_H)=n, \quad \Delta_H=0\,. \tag{3.34}$$

This result describes the effect of velocity diffusion and simultaneous rf excitation on the velocity distribution of Hertzian coherence. In an intuitive interpretation, the first term on the right-hand side of (3.33) can be identified with the contribution of those optically pumped atoms that have not yet undergone velocity-changing collisions: Their average interaction time with the rf field is of the order of $1/(\gamma_g+\gamma_{VCC})$ which leads to a damping constant of $\gamma_g+\gamma_{VCC}$ in the common resonance denominator of (3.33), and to a correspondingly large rf resonance linewidth in the signal contribution of this term. We also note that the summands in the second term of (3.33) display the average effect of n collisions on the atomic rf excitation; the related resonance denominators of (3.34) are raised to the nth power, indicating that the sum terms show smaller rf resonance linewidths resulting from longer rf-atom interaction times. The second term in (3.33) also describes the velocity diffusion of $\tilde{\rho}_{12}(v)$ through the factors $K_n(v,v')$ whose structure is given by (3.31). In turns out from (3.31) and (3.33) that the summands in the second term of (3.33) describe the partially thermalized, optically off-resonant parts of $\tilde{\rho}_{12}(v)$: These contributions that show small rf resonance linewidths correspond to atoms that have experienced several VCC during their rf excitation. It may be noted in this context that the velocity distribution of rf-excited atoms shown in Fig. 3(a) displays the velocity dependence of the imaginary part of $-\tilde{\rho}_{12}(v)$ for $\Delta_H=0$.

3. *The resulting modulation depths*

It has just been shown how the expected rf resonance linewidths depend on the probed velocity subgroup, and hence on the velocity selectivity of the optical detection process. In our case, the calculation of m_{AM} and m_{FM} with the use of (3.19), (3.22f), (3.23b), and (3.23c) directly yields the velocity selectivities of AM- and FM-RHS. We obtain the following expressions for the AM and FM modulation parameters:

$$m_{AM}=\frac{kL}{\epsilon_0}\frac{\mu_E}{\sqrt{2}}\frac{i\beta_E}{E_0}\left\langle\tilde{\rho}_{21}(v)\frac{\Gamma-i\Delta_H}{(kv_0-kv)^2-(i\Gamma+\Delta_H)^2}\right\rangle, \tag{3.35a}$$

$$m_{FM}=\frac{kL}{\epsilon_0}\frac{\mu_E}{\sqrt{2}}\frac{i\beta_E}{E_0}\left\langle\tilde{\rho}_{21}(v)\frac{kv_0-kv}{(kv_0-kv)^2-(i\Gamma+\Delta_H)^2}\right\rangle. \tag{3.35b}$$

It turns out that the AM and FM detection sensitivities given by the second factor in the angular brackets of (3.35a) and (3.35b) have an absorptive and dispersive shape, respectively, with regard to the optically resonant subgroup of velocity v_0. Independent of all approximations made in the calculation of the RHS, this fact is a direct consequence of the inherent symmetry present in the considered type of level system.

It is clear from (3.55a) that the AM-RHS is proportional to the optically resonant part of the sublevel coherence velocity distribution with a velocity resolution that is related to the homogeneous optical linewidth. As a result, the shape of the AM-RHS detection sensitivity is matched to the no-collision contribution in $\tilde{\rho}_{12}(v)$ as given by the first term in (3.33). In contrast, the FM-RHS (3.35b) is sensitive to the VCC-induced asymmetry in the optically off-resonant wings of the distribution (3.33). This specific behavior of AM- and FM-RHS is also illustrated in Fig. 3.

In the limit of small rf detunings $\Delta_H\ll\Gamma$, the velocity integration of (3.35) can easily be carried out with the use of the w function,[19]

$$w(z)=\frac{i}{\pi}\int\frac{e^{-t^2}}{z-t}dt, \quad \mathrm{Im}(z)>0 \tag{3.36}$$

and its properties

$$w(-z^*)=w^*(z)\,, \tag{3.37a}$$

$$w'(z)=-\frac{i}{\pi}\int\frac{e^{-t^2}}{(z-t)^2}dt=-2zw(z)+\frac{2i}{\sqrt{\pi}}\,, \tag{3.37b}$$

$$w(z)\simeq e^{-z^2}\left[1+\frac{2iz}{\sqrt{\pi}}\right], \quad z\to 0\,. \tag{3.37c}$$

The expression resulting for the in-phase component of m_{AM} is

$$\mathrm{Re}(m_{AM})=-\frac{\sqrt{\pi}N}{u}\exp\left[-\left[\frac{v_0}{u}\right]^2\right]\frac{L\mu_E^4}{6\sqrt{2}\epsilon_0\hbar^4\Gamma}\left[\frac{E_0}{2}\right]^2\frac{B_H}{2}\frac{\mu_H}{(\gamma_g+\gamma_{VCC})^2+\Delta_H^2}$$
$$\times\left\{W_0^{AM}(v_0)+\sqrt{\pi}\frac{2\Gamma}{ku}\sum_{n=1}^{\infty}\left[\frac{W_n^{AM}(v_0)}{(1-\alpha^{2n})^{1/2}}\left[\frac{\gamma_{VCC}}{[(\gamma_g+\gamma_{VCC})^2+\Delta_H^2]^{1/2}}\right]^n\left[\cos(n\delta)+\frac{\gamma_g+\gamma_{VCC}}{\Delta_H}\sin(n\delta)\right]\right]\right\}, \tag{3.38a}$$

and $\mathrm{Re}(m_{\mathrm{FM}})$ is obtained with the formal replacement of W_n^{AM} by W_n^{FM} in (3.38a):

$$\mathrm{Re}(m_{\mathrm{FM}})=[\mathrm{Re}(m_{\mathrm{AM}})]_{W_n^{\mathrm{AM}}\to W_n^{\mathrm{FM}}} . \tag{3.38b}$$

Here δ, W_n^{AM}, and W_n^{FM} are defined by

$$\delta\equiv\arctan\left[\frac{\Delta_H}{\gamma_g+\gamma_{\mathrm{VCC}}}\right], \tag{3.38c}$$

$$W_n^{\mathrm{AM}}(v_0)+iW_n^{\mathrm{FM}}(v_0) \equiv w\left[(1-\alpha^{2n})^{-1/2}\left[i\frac{\Gamma}{ku}+(1-\alpha^n)\frac{v_0}{u}\right]\right], \quad n\geq 1 . \tag{3.38d}$$

In the limit of a strongly Doppler-broadened optical transition ($ku\gg\Gamma$), one can use the expansion (3.37c) to approximate

$$\mathrm{Re}\left[w\left[i\frac{\Gamma}{ku}+\frac{v_0}{u}\right]\right]\simeq\exp\left[-\left[\frac{v_0}{u}\right]^2\right], \quad \Gamma\ll ku \tag{3.39}$$

and then finally obtain for W_0^{AM} and W_0^{FM} the simple expressions

$$W_0^{\mathrm{AM}}(v_0)=1 , \tag{3.40a}$$

$$W_0^{\mathrm{FM}}(v_0)=\frac{2\Gamma}{ku}\frac{v_0}{u} . \tag{3.40b}$$

C. Discussion of theoretical results

Our calculations predict that the line shapes of the rf resonance signals are determined not only by depolarizing collisions, but also by VCC. We now show how this fact is reflected in the differences between AM and FM Raman heterodyne signals. Moreover, the influence of relaxation parameters on the line shapes will be discussed in some detail.

The most obvious difference between AM and FM signals appears in their dependence on the optical detuning with respect to the center of the Doppler profile, kv_0, in the case of resonant rf excitation ($\Delta_H=0$). Using the symmetry property (3.37a), Eqs. (3.38a) and (3.38b) can be written in the form

$$\mathrm{Re}(m_{\mathrm{AM}})=C_{\mathrm{AM}}\exp\left[-\left[\frac{v_0}{u}\right]^2\right], \tag{3.41a}$$

$$\mathrm{Re}(m_{\mathrm{FM}})=C_{\mathrm{FM}}\frac{v_0}{u}\exp\left[-\left[\frac{v_0}{u}\right]^2\right], \tag{3.41b}$$

where the remaining v_0 dependence of C_{AM} and C_{FM} is symmetric in v_0. Thus, the AM- and FM-RHS depend on the laser detuning kv_0 analogously to Doppler-broadened optical absorption and dispersion, respectively. We note that this behavior is a consequence of the absorptive and dispersive detection sensitivities derived in (3.35).

Let us now consider the dependence of the rf resonance line shapes of AM- and RM-RHS on the characteristic parameter $G=\gamma_{\mathrm{VCC}}/\gamma_g$ that gives the average number of VCC during the lifetime of the Hertzian coherence. Experimentally, this parameter is expected to depend on the studied system as well as on the density of collision partners.

(i) $G=0$. This limit is given in the collisionless case if the decay rate γ_g describes the relaxation due to thermal motion;[4] on the other hand, it can be expected that $G=0$ also describes the case that the velocity changes connected with sublevel coherence-preserving collisions are too small to remove the active atoms from optical resonance ($k\Delta u\ll\Gamma$). For $G=0$, AM- and FM-RHS are given by the first term of (3.38a) and (3.38b),

$$\mathrm{Re}(m_{\mathrm{AM}})=K\frac{1}{\gamma_g^2+\Delta_H^2}\exp\left[-\left[\frac{v_0}{u}\right]^2\right], \tag{3.42a}$$

$$\mathrm{Re}(m_{\mathrm{FM}})=K\frac{1}{\gamma_g^2+\Delta_H^2}\frac{2\Gamma}{ku}\frac{v_0}{u}\exp\left[-\left[\frac{v_0}{u}\right]^2\right] . \tag{3.42b}$$

In this approximation, both AM and FM signals show Lorentzian resonances of width $\Delta\omega_{1/2}=\gamma_g$ [half width at half maximum (HWHM)]. The amplitude of the FM-RHS is smaller by the factor $2\Gamma/ku$ ($v_0=u$) since it results only from the slight asymmetry of the optically pumped velocity packet that is present for $v_0\neq 0$. It has to be mentioned, however, that the calculated weak FM-RHS (3.42b) can be easily masked by small contributions of the AM-RHS present during FM detection. Such "crosstalk" may in particular originate from phase shifts of the local oscillator field $\mathbf{E}_0$ with respect to $\mathbf{E}_\pm$ caused by propagation effects. A non-negligible contribution to the FM-RHS in the collisionless case can also arise from radiation-induced velocity changes (photon impact).[10]

(ii) $G<1$. For the AM signal, the first term in (3.38a) is still dominant which leads to rf resonances of width $\Delta\omega_{1/2}=\gamma_g+\gamma_{\mathrm{VCC}}$ (see left part of Fig. 4); the broadening caused by VCC is a result of a velocity diffusion-limited time of observation of the active atoms and can thus be understood as a transit-time broadening in velocity space. In contrast, numerical calculations show that for $v_0\leq u$, the resulting FM linewidth is close to $\Delta\omega_{1/2}=\gamma_g$ ($\pm 10\%$) for a broad range of physically reasonable values of the parameters G, Γ/ku, and α. This behavior leads us to assume that the linewidth of the FM-RHS is largely independent of the type of collision kernel that describes the velocity-change spectrum. With respect to the amplitude of the weak FM-RHS, we note that its value is increased for $kv_0\neq 0$ by the partly thermalized, off-resonant parts of $\tilde{\rho}_{12}(v)$ that correspond to the sum terms of (3.38b).

(iii) $G\geq 1$. Depending on the values of Γ/ku and α, the sum terms of (3.38a) now begin to contribute to m_{AM}. This corresponds to the onset of velocity diffusion directed back into the resonant velocity subgroup, leading to a reduction of the AM-RHS broadening ($\Delta\omega_{1/2}<\gamma_{\mathrm{VCC}}+\gamma_g$) and also to characteristic non-Lorentzian rf resonant line shapes (see Fig. 5). The calculations show that the efficiency of reverse velocity diffusion in limiting the AM-RHS linewidths strongly depends on the values of the parameters α and Γ/ku. It follows from this that the AM-RHS rf resonance linewidths can be reduced by a broadening of the homogeneous optical linewidth for $G\geq 1$; on the other hand, the AM-RHS linewidths are now also influenced by the shape of the collision kernel and especially

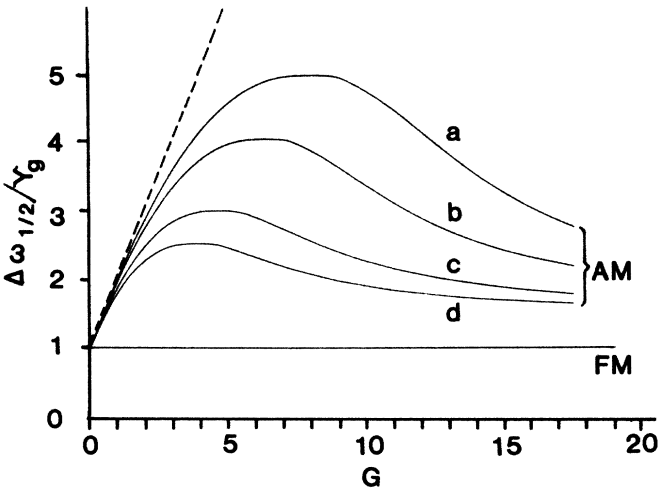

FIG. 4. Calculated rf resonance linewidths (HWHM) $\Delta\omega_{1/2}/\gamma_g$ of AM- and FM-RHS for $v_0=u$ as a function of $G=\gamma_{VCC}/\gamma_g$. The parameter values are (a) $\alpha=0.96$, $\Gamma/ku=0.002$; (b) $\alpha=0.98$, $\Gamma/ku=0.002$; (c) $\alpha=0.96$, $\Gamma/ku=0.005$; (d) $\alpha=0.98$, $\Gamma/ku=0.005$. The variations of the FM-RHS linewidths are too small to be seen in the figure. In the limit $G\to 0$, the AM-RHS linewidths are equally broadened according to $\Delta\omega_{1/2}=\gamma_{VCC}+\gamma_g$ as described by the dashed line.

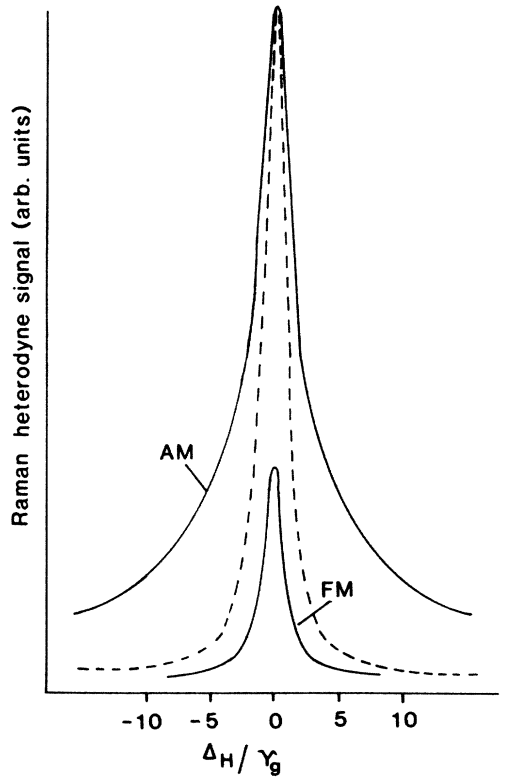

FIG. 5. Calculated rf resonance line shapes of AM- and FM-RHS (solid lines) as a function of normalized rf detuning Δ_H/γ_g under conditions of VCC; parameter values are $\gamma_{VCC}/\gamma_g=10$, $\Gamma/ku=0.01$, $\alpha=0.98$, $v_0/u=1$. A Lorentzian of width γ_g (dashed line) is shown for comparison.

by the average magnitude of the collisional velocity changes.

(iv) $G\gg 1$. The sum series of (3.38a) and (3.38b) now converges very slowly and both AM- and FM-RHS mainly depend on terms with *large* n values. In this case, we can use the approximations

$$(1-\alpha^{2n})^{1/2}\simeq 1,\quad n\to\infty \tag{3.43}$$

and

$$W_n^{AM}(v_0)+iW_n^{FM}(v_0)\simeq w\left[i\frac{\Gamma}{ku}+\frac{v_0}{u}\right],\quad n\to\infty\ . \tag{3.44}$$

In the limit given by $G^2\gg ku/\Gamma$, the summation in (3.38a) and (3.38b) can now be carried out analytically which yields the following simple expressions for the modulation parameters:

$$\mathrm{Re}(m_{AM})\simeq K\exp\left[-\left[\frac{v_0}{u}\right]^2\right]\frac{2\Gamma}{ku}\times\mathrm{Re}\left[w\left[i\frac{\Gamma}{ku}+\frac{v_0}{u}\right]\right]\frac{1}{\gamma_g^2+\Delta_H^2}\ , \tag{3.45a}$$

$$\mathrm{Re}(m_{FM})\simeq K\exp\left[-\left[\frac{v_0}{u}\right]^2\right]\frac{2\Gamma}{ku}\times\mathrm{Im}\left[w\left[i\frac{\Gamma}{ku}+\frac{v_0}{u}\right]\right]\frac{1}{\gamma_g^2+\Delta_H^2}\ . \tag{3.45b}$$

It can thus be expected that both AM- and FM-RHS linewidths are again well approximated by $\Delta\omega_{1/2}=\gamma_g$ in the case of nearly complete thermalization of the Hertzian coherence velocity distribution. In contrast to the case $G=0$, however, the amplitude ratio $|m_{AM}/m_{FM}|$ may now come close to unity, as can be seen from (3.45a) and (3.45b) with the use of (3.37c). In practice, the limit of (3.45) should be valid, e.g., for the ground states of alkali-metal atoms and rare-gas collision partners where the probability of collisional depolarization is known to be extremely low.[6]

IV. EXPERIMENT

Our experiments were carried out in atomic samarium vapor in the presence of rare-gas perturbers. The Sm $\lambda=570.7$ nm $4f^6 6s^2\,{}^7F_1-4f^6 6s\,6p\,{}^7F_0$ line was used for optical excitation: In the presence of a static magnetic field, the even ($I=0$) Sm isotopes here posses the simple level system shown in Fig. 1(b). The effect of collisions on AM- and FM-RHS was studied in the experiments with the use of He, Ne, Ar, and Xe perturber atoms at various number densities. After a brief description of the experimental setup, we present the basic features of the experimentally observed RHS and display in detail the measured rare-gas pressure dependence of the rf resonance line shapes.

A. Experimental setup

The schematic of the experimental apparatus has already been shown in Fig. 1(a). We used a homebuilt cw

single-mode dye ring laser with a short-time linewidth of 0.2–1 MHz (HWHM). The approximately Gaussian output beam (diameter for $1/e$ intensity drop: $d \simeq 1$ mm) was attenuated by neutral-density filters and then directed through a polarizer in front of the Sm cell to define a direction of polarization parallel to the static magnetic field $\mathbf{B}_0$ (π light). Behind the Sm cell, the resulting carrier and Raman sideband fields passed through a low-order $\lambda/4$ quartz plate that was carefully aligned to have its slow axis parallel to the polarization of the carrier field and to yield the required phase retardation of $\theta = 90°$; the polarization analyzer was inserted with $\phi = 45°$. With this scheme, the FM-RHS could be recorded; for the detection of the generally stronger AM-RHS, a phase retardation of $\theta = 0$ was obtained by placing an additional $\lambda/4$ plate in front of the analyzer to compensate the effect of the first retardation plate. As a result, AM- and FM-RHS could be measured subsequently without degrading the precise optical alignment that was necessary to isolate the FM-RHS. Crosstalk effects due to remaining optical imperfections led to a detection limit for weak FM signals that corresponds to an amplitude ratio of AM- and FM-RHS of $| m_{\mathrm{AM}}/m_{\mathrm{FM}} | \simeq 300$.

Natural Sm consists of a mixture of seven isotopes with mass numbers 144, 147, 148, 149, 150, 152, and 154; according to the Landé factor of $g_J = 1.50$ for the $J = 1$ ground state of the even Sm isotopes,[20] the Zeeman splitting of the m sublevels is given by a Bohr frequency of $\Omega_H \simeq B_0$ $(2\pi \times 21$ MHz)/mT. Using cell temperatures of 900–1100 K, the resonant small-signal absorption of the Doppler broadened ($ku \simeq 2\pi \times 700$ MHz) ^{154}Sm transition had a typical value of 10% which corresponds to a ^{154}Sm number density of $N \simeq 4 \times 10^{12}$ cm^{-3}. For these number densities, propagation effects in the sample and Sm-Sm collisions had no influence on the line shapes of the Raman heterodyne signals.

The Sm vapor was contained in an aluminum oxide ceramic tube 20 cm in length and 1 cm in diameter. The cell was placed between a pair of Helmholtz coils that generated the static magnetic field $\mathbf{B}_0$; the earth's magnetic field was compensated for by a small additional magnetic field. The fused quartz cell windows were held by brass fittings mounted on the ends of the ceramic tube, with one of the window holders also serving as a connection to the vacuum and rare-gas handling system. Depending on the pressure range, the rare-gas pressure was measured with a thermoelectric instrument calibrated by a McLeod pressure gauge, or with a capacitance manometer. The ceramic tube was heated in its central part over a length $L = 3$ cm and water cooled at its ends. In order to rule out signal contributions due to the magnetic stray field of the heating elements, the heating current was pulsed in 10-ms intervals with the output of the photodetector being electronically blocked during these times.

The rf magnetic field of frequency $\omega_H \simeq 2\pi \times 20$ MHz was produced by a coil 8 cm in length and 10 cm in diameter that was centered to the optical interaction region. The coil was part of a resonantly tuned LC circuit driven by a rf power amplifier; the amplifier input voltage and the rf lock-in reference signal were supplied by a frequency synthesizer. The whole Sm cell, except for its windows, was surrounded by a 1-mm copper shielding to prevent rf pickup in the detection system. With a rf input power of 20 mW, the resulting magnetic field amplitude in the interaction region was $B_H \simeq 2$ μT, a sufficiently small value to exclude rf saturation effects.

The optical heterodyne beat signal was generated in a fast p-i-n photodiode connected to a 30-dB rf preamplifier. Before reaching the rf lock-in amplifier input, the heterodyne signal passed a diode switch controlled by the heating current (see above) and a band pass device (bandwidth $\Delta\nu \simeq 3$ MHz) used to prevent an overload of the rf lock-in amplifier (Princeton 5202) with wideband noise. For the measurement of rf resonance signals, the rf detuning was varied by sweeping the static magnetic field $\mathbf{B}_0$ at a fixed value for ω_H. Alternatively, the laser frequency ω_E could be swept to obtain the dependence of the RHS on the laser detuning kv_0 with respect to the Doppler-broadened optical transition. The signal averaging was performed by a minicomputer.

B. Measurements

In Fig. 6, AM- and FM-RHS are shown as a function of laser frequency under conditions of resonant rf excitation ($\Delta_H = 0$). The AM-RHS clearly shows the Doppler-broadened contributions of the five even Sm isotopes with

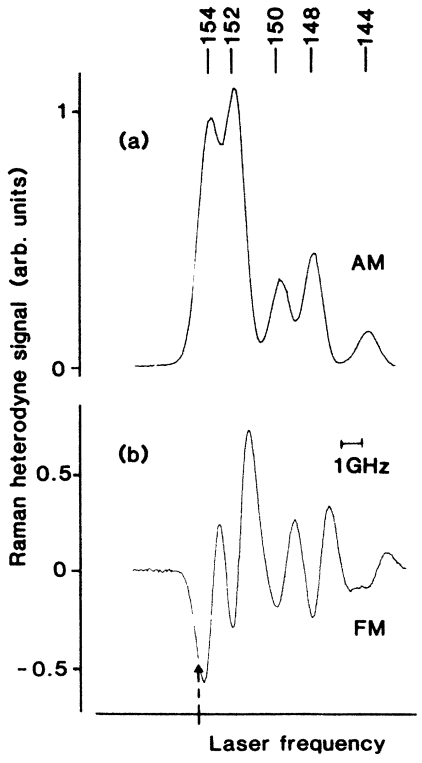

FIG. 6. Measured in-phase components of AM-RHS (a) and FM-RHS (b) as a function of laser frequency under conditions of resonant rf excitation ($\Delta_H = 0$). The signal contributions of the various even Sm isotopes are indicated. The He buffer-gas pressure was $p_{\mathrm{He}} = 3.0$ mbar. For arrow see text.

the relative peak heights being determined by the natural isotope abundancy;[21] the odd ^{147}Sm and ^{149}Sm isotopes have largely different rf resonance frequencies and yield no contributions to the measured RHS. It may be noted in this context that a measurement of the AM-RHS in dependence on laser frequency can be used for a sensitive, background-free detection of weak, Doppler-broadened absorption. Here, the resonant rf excitation can serve as a kind of tracer discriminating various species as, e.g., even and odd isotopes.

The comparison of AM- and FM-RHS suggests the conclusion that the AM signal varies similar to Doppler-broadened optical absorption and that the FM-RHS has the derivativelike shape of the corresponding optical dispersion: This behavior has been predicted by (3.42) as a consequence of the absorptive and dispersive detection sensitivities connected with AM and FM Raman heterodyne detection, respectively. We also note that both RHS here have comparable maximum amplitudes; it will become clear below that this fact is related to the high He-buffer-gas pressure of $p=3.0$ mbar used for the measurement shown in Fig. 6.

Raman heterodyne signals as a function of the rf detuning Δ_H (rf resonance signals) were obtained with a constant nonzero laser detuning of $kv_0 \simeq -ku$ with respect to the ^{154}Sm transition as indicated by the arrow in Fig. 6. This allowed us to obtain both AM- and FM-RHS under identical experimental conditions; the in-phase components of the corresponding rf resonance signals now have the shape of resonance peaks of opposite polarity for AM- and FM-RHS (see Fig. 6). As one example, we show in Fig. 7 typical experimental signals that display the variation of the rf resonance linewidths and signal amplitudes of AM- and FM-RHS with increasing He pressure: Without Sm-He collisions ($p_{He}=0$ mbar), both AM and FM signals have equal linewidths; according to the Landé factor given above, these linewidths correspond to $\Delta\omega_{1/2} \simeq 2\pi \times 150$ kHz (HWHM). For $p_{He}=0.09$ mbar, the AM-RHS linewidth is increased by almost a factor of 2 while the FM width is now $\Delta\omega_{1/2} \simeq 2\pi \times 115$ kHz; finally, the RHS recorded at $p_{He}=0.5$ mbar shows that the linewidth of the AM-RHS is again reduced to a value close to the no-collision linewidth, and that there is only little change in the width of the FM-RHS. From the scale factors given in Fig. 7 and from Fig. 8, it can also be seen that the amplitude ratio $|m_{AM}/m_{FM}|$ decreases drastically with buffer-gas pressure mainly as a result of a decreasing AM-RHS amplitude.

The measured He pressure dependence of the rf resonance linewidths of AM- and FM-RHS is shown by the data points in Fig. 9(a); the corresponding results obtained with Ne, Ar, and Xe perturbers are shown in Fig. 9(b), 9(c), and 9(d), respectively. In all cases, we observe a qualitatively similar behavior of the FM-RHS linewidths and a sharp increase of the AM-RHS linewidths at low pressures. The pressure dependence of the AM linewidths at large pressures, however, shows characteristic variations for the different collision partners. In particular, the distinct maximum observed in the AM-RHS linewidth for Helium collision partners is absent for the heavier rare gases; here, the linewidth of the AM-RHS remains considerably larger than that of the FM signal also in the case of high pressures.

During our measurements, the optical power density of the laser field was kept at 600 μW/mm^2 ($\pm 20\%$) except for the case of zero rare-gas pressure. In the latter case, the cell entrance window got slightly covered with condensing Sm vapor and the intensity was effectively re-

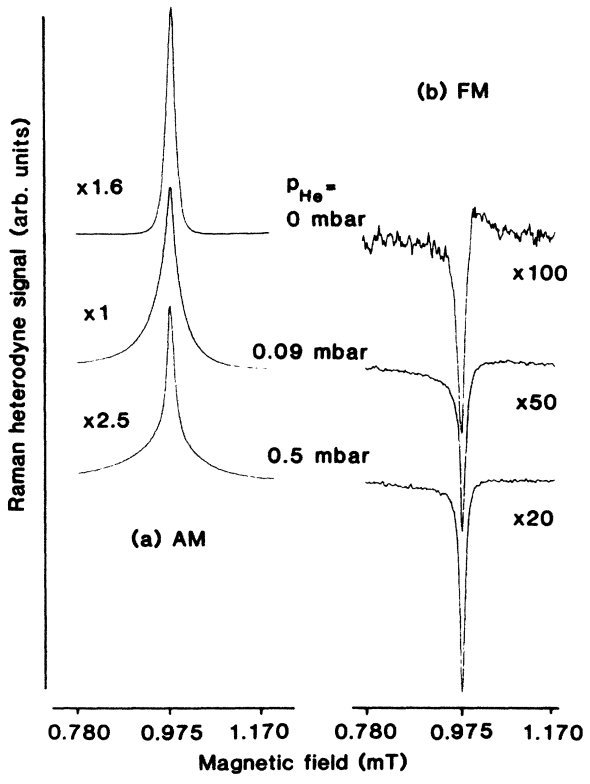

FIG. 7. Measured in-phase AM-RHS (a) and FM-RHS (b) as a function of static magnetic field $\mathbf{B}_0$ (rf resonance signals) for three values of He pressure. For other experimental parameters see text.

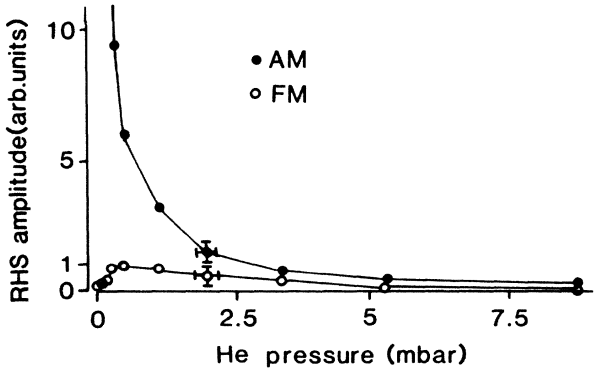

FIG. 8. Measured magnitudes (arbitrary units) of AM- and FM-RHS for $kv_0 \simeq -2\pi \times 700$ MHz and $\Delta_H=0$ as a function of He pressure. The lines between the data points are a guide to the eye; typical error bars are indicated.

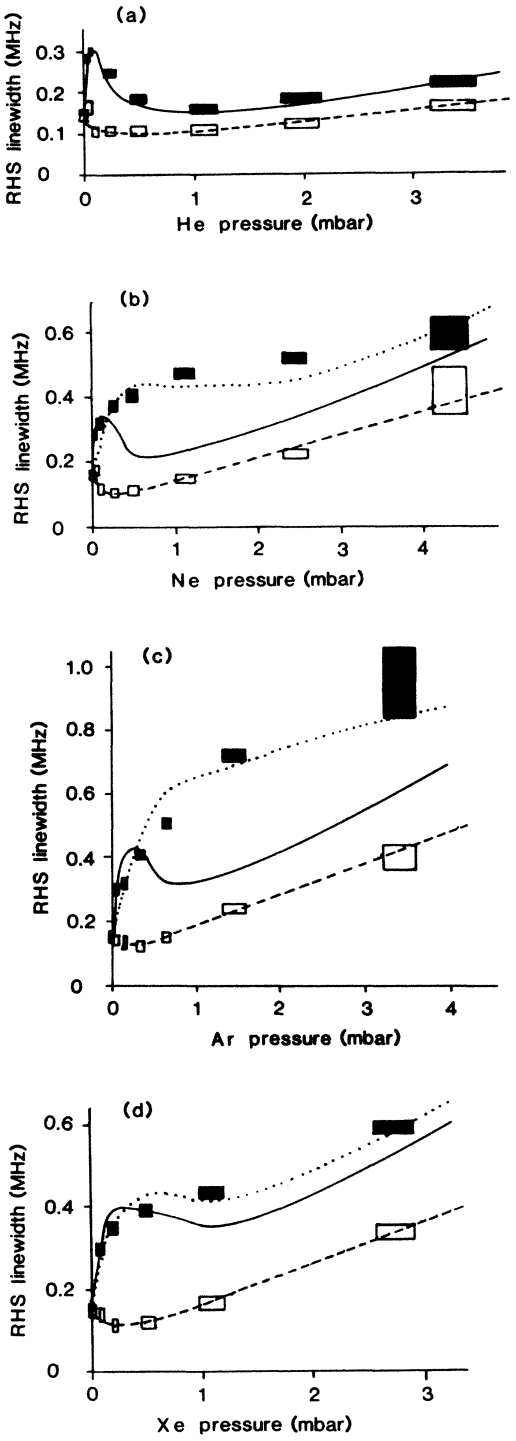

FIG. 9. Measured pressure dependence of AM-RHS linewidths (solid squares) and of FM-RHS linewidths (open squares) for He (a), Ne (b), Ar (c), and Xe (d) rare-gas collision partners. The solid and dotted lines correspond to numerically calculated AM-RHS linewidths (see text) for different parameter values: He (——), $\gamma_{VCC}=30\times10^6\ s^{-1}mbar^{-1}$, $\alpha=0.985$; Ne (——), $\gamma_{VCC}=19\times10^6\ s^{-1}mbar^{-1}$, $\alpha=0.97$; Ne (· · ·), $\gamma_{VCC}=9\times10^6\ s^{-1}mbar^{-1}$, $\alpha=0.94$; Ar (——), $\gamma_{VCC}=19\times10^6 s^{-1}mbar^{-1}$, $\alpha=0.96$; Ar (· · ·), $\gamma_{VCC}=9\times10^6\ s^{-1}mbar^{-1}$, $\alpha=0.93$; Xe (——), $\gamma_{VCC}=13.5\times10^6\ s^{-1}mbar^{-1}$, $\alpha=0.95$; Xe (· · ·), $\gamma_{VCC}=11\times10^6\ s^{-1}\ mbar^{-1}$, $\alpha=0.95$. Dashed lines: see text.

duced to $\simeq 250\ \mu W/mm^2$. The FM-RHS linewidths at low pressures ($p<0.5$ mbar) and the AM linewidth at $p=0$ mbar increased when the laser beam diameter was reduced by means of an aperture; this indicates that they were determined by transit-time effects. We also note that for intermediate rare-gas densities ($p=0.2$–0.5 mbar), the AM-RHS linewidths decreased with increasing optical power while the FM linewidths remained approximately constant. An explanation of this interesting phenomenon will be given below.

V. DISCUSSION

Here we first give a qualitative interpretation for the experimentally observed pressure dependence of the rf resonance line shapes; we especially show how the rate constants for VCC and depolarizing collisions can be derived separately from such experimental data. In a second step, the validity of our theoretical description is tested quantitatively by direct comparison of experimentally observed and calculated RHS linewidths. We finally discuss the collisional cross sections and collision kernel parameters that are obtained from the measurements and calculations.

A. Pressure dependence of rf resonance line shapes

The distinctly different pressure dependence of AM- and FM-RHS line shapes can be understood by recalling the theoretical predictions on the influence of collisional velocity diffusion and sublevel coherence decay on the line shapes of the Raman heterodyne signals (see Sec. III C), and by considering the pressure dependence of the corresponding rate constants γ_{VCC} and γ_g that is qualitatively outlined in Fig. 10.

(i) *FM-RHS linewidths.* Theory predicts that the FM-RHS linewidth is given in a good approximation by $\Delta\omega_{1/2}=\gamma_g$, where γ_g is the time rate that describes the decay of ground-state population difference and Hertzian coherence. In our case, this decay rate has two contributions of opposite pressure dependence (see Fig. 10) that result from depolarizing collisions (γ_c) and from diffusive thermal motion through the optical interaction region (transit time, γ_{tr}). At large pressures, we have $\gamma_g\simeq\gamma_c$; we observe a linear increase of the FM-RHS linewidths with pressure as a result of the rising time rate of depolarizing collisions. The corresponding rate constant γ_c thus can be derived directly with only small systematic errors from the increase of the FM-RHS linewidths at high perturber densities. For low pressures, the transit-time broadening yields significant contributions and the measured FM-RHS linewidths show relatively small variations due to the opposite pressure dependence of γ_c and γ_{tr}. Let us also mention that in the limit of very low perturber densities and a correspondingly weak VCC-induced FM signal, the measured FM-RHS linewidths can be easily influenced by signal contributions that originate from "crosstalk" between AM- and FM-RHS. In our FM-RHS linewidth data, slightly increased values for $\Delta\omega_{1/2}$ at the lowest nonzero He and Ne pressure in Figs. 9(a) and 9(b) in fact indicate the presence of small crosstalk contribu-

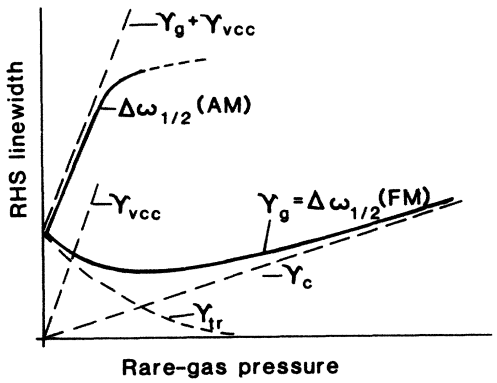

FIG. 10. Outline of the pressure dependence of the transit-time decay rate (γ_{tr}), of the rate of depolarizing collisions (γ_c), and of the VCC rate constant γ_{VCC}. The pressure dependence of the FM-RHS linewidths is determined by $\Delta\omega_{1/2}(FM)=\gamma_g=\gamma_{tr}+\gamma_c$; for low rare-gas pressures, the AM-RHS linewidths increase according to $\Delta\omega_{1/2}(AM)=\gamma_{VCC}+\gamma_g$.

tions in the detected FM-RHS (see below).

(ii) *AM-RHS linewidths.* Our calculations show that the AM-RHS linewidths strongly depend on the ratio of rate constants $G=\gamma_{VCC}/\gamma_g$ that gives the average number of VCC during the sublevel coherence lifetime. In our experiment, the characteristic parameter G is given at low pressures ($\gamma_{tr}>\gamma_c$, see Fig. 10) by the average number of VCC during the beam transit time ($G=\gamma_{VCC}/\gamma_{tr}$), and it rises with increasing pressure to the limiting value $G=\gamma_{VCC}/\gamma_g$ that only depends on the collision partners involved. The possible strong variation of G with perturber density is most instructively illustrated with the He pressure dependence of the AM-RHS linewidths shown in Fig. 9(a). The rapid increase of G with buffer-gas pressure leads to an initial sharp rise and a subsequent decrease of the measured linewidths; the reduction of the AM-RHS linewidths to values close to those of the FM-RHS at large He pressures indicates a nearly complete thermalization in the velocity distribution of Hertzian coherence ($G\gg1$).

At low pressures, the condition $G<1$ is fulfilled for all studied rare gases and the commonly observed strong initial pressure broadening of the AM-RHS is the result of a correspondingly strong increase of γ_{VCC} with perturber density. If the pressure variations of γ_g can be neglected, it is thus possible to derive the time rate of velocity-changing collisions directly from the low-pressure increase of the AM-RHS rf resonance linewidths (see Fig. 10).

The further rise of rare-gas pressure then yields $G\geq1$ and the resulting onset of reverse velocity diffusion leads to a reduction of the initial broadening ($\Delta\omega_{1/2}<\gamma_{VCC}+\gamma_g$) and to the predicted development of pronounced wings in the line shape of the AM-RHS as can be seen in Fig. 7 for $p_{He}=0.5$ mbar. It is clear that the pressure dependence of the AM-RHS linewidths is for $G\geq1$ also influenced in a complicated manner by the width and structure of the velocity-change spectrum and by the pressure broadening of the homogeneous optical linewidth. Considering our theoretical predictions (see Fig. 4), the observed reduction of the AM-RHS linewidths due to large optical power densities can be easily explained as a consequence of the power broadening of the effective optical linewidth.

(iii) *RHS amplitudes.* For $|kv_0|=ku$, we expect a decrease of the RHS amplitude ratio from $|m_{AM}/m_{FM}|=ku/2\Gamma$ in the collisionless case to values close to one for $G\gg1$. In our measurements, the nearly complete thermalization of the velocity distribution of Hertzian coherence at large He pressures in fact leads to $|m_{AM}/m_{FM}|\simeq1.5$ for $p_{He}=3.0$ mbar (see Fig. 6); the overall shape of the measured pressure dependence of m_{AM} and m_{FM} (see Fig. 8) is in good agreement with calculations. Only for zero rare-gas pressure, a significant disagreement exists between the measured value of $|m_{AM}/m_{FM}|\simeq63$ (see Fig. 7) and the predicted (3.42) upper limit of $|m_{AM}/m_{FM}|=ku/2\Gamma=1.5\times10^3$ [$ku=2\pi\times700$ MHz, $\Gamma=2\pi\times0.23$ MHz (Ref. 22)]. We have found that this discrepancy is due to the fact that the FM-RHS measured at $p=0$ mbar is dominated by a small crosstalk signal; this crosstalk signal is proportional to the AM-RHS and is related to the slightly different transverse dimensions of the copropagating laser and Raman sideband fields.[10] Our experimental results clearly demonstrate, however, that the crosstalk signal is sufficiently weak to be neglected with respect to the VCC-induced FM-RHS even in the case of only low densities of collision partners.

B. Numerical calculations

The experimental data (see Fig. 9) show that the pressure dependence of the AM-RHS linewidths at large pressures ($p>0.2$ mbar) is characteristically different for He, Ne, Ar, and Xe perturbers, indicating a corresponding difference in the influence of collisions on the Raman heterodyne signals. From a general point of view, this fact is not surprising since the spectrum of collisional velocity changes and the efficiency of collisional depolarization are related to the shape of the state-dependent interatomic potential[8] and to the mass ratio of active and perturber atoms. Our phenomenological theoretical model, however, is not based on a physical potential and uses the formally independent parameters γ_g, γ_{VCC}, α, and Γ to take into account the effects of collisions. In the following, the possible accuracy of this approach in describing quantitatively the entire shape of the measured AM-RHS pressure broadening is tested by numerical calculations. As a particular result of such calculations, we expect to obtain some information on the width of the collision kernels $W(v'\rightarrow v)$ and on the adequacy of the Keilson-Storer model for the considered case of Sm—rare-gas collisions.

Our numerical calculations are based on Eq. (3.38) and use an appropriate and consistent choice of the collision parameters. The rate constant γ_g is derived from the smoothed values of the experimental FM-RHS linewidths as given by the dashed lines in Fig. 9; the values of γ_{VCC} are chosen to be proportional to pressure with an increase

matching the initial broadening ($p<0.1$ mbar) of the AM-RHS.

We further assume an effective optical linewidth $\Gamma'=(\Gamma^2+\Gamma_p^2)^{1/2}$ to describe the width of the optically resonant velocity ensemble. We here take into account the pressure-dependent decay rate of optical coherence $\Gamma=\Gamma_4/2+\Gamma_c$; also, for $p\leq 1$ mbar, there is a residual power broadening of the optical excitation (Γ_p) that can be calculated with an approximated nonperturbative solution of (3.22a)–(3.22d).[18] To describe the pressure broadening of the homogeneous optical linewidth, we set $\Gamma_c\geq\gamma_{\rm VCC}$, where Γ_c is the total dephasing rate of optical coherence due to collisional velocity changes and due to the state dependence of the collisional interaction potential.[15] The values of Γ_c that are proportional to pressure and the pressure-independent values of the collision kernel parameter α were chosen for optimum agreement between calculated and measured AM-RHS linewidths.

The resulting calculated AM-RHS linewidths are shown as solid lines in Fig. 9. In the case of He, a suitable choice of the free parameters (see the figure caption) yields calculated AM-RHS linewidths that agree almost entirely with the measured values in the limits of their experimental uncertainty. Significant discrepancies, however, arise especially for Ne and Ar where the calculated linewidths are significantly smaller than the measured values for high rare-gas pressures. We have found that this behavior is independent of the choice of α and Γ_c as long as the physically reasonable condition $\Gamma_c\geq\gamma_{\rm VCC}$ is not violated. A satisfactory overall agreement is possible only if values of $\gamma_{\rm VCC}$ are used that lie below those derived from the initial pressure broadening of the AM-RHS. The corresponding calculated AM-RHS linewidths are shown as dotted lines in Figs. 9(b), 9(c), and 9(d). In all fitting attempts, the assumption of a collisional broadening of the homogeneous optical linewidth according to $\Gamma_c=\gamma_{\rm VCC}$ resulted in the best agreement of experimental and calculated linewidths.

To give an explanation for the observed discrepancies between measured and calculated AM-RHS linewidths, let us note that our theoretical model assumes, by making the approximation $k\Delta u\gg\Gamma$ for the width of the Gaussian collision kernel, that the velocity-change spectrum contains a negligible contribution of collisional velocity changes that lie below the experimental limit of velocity resolution given by the homogeneous optical linewidth Γ. In fact, the values of the collision parameters used in the numerical calculations are always consistent with the condition $k\Delta u\gg\Gamma$, thereby suggesting that the decrease of velocity resolution at large pressures due to the pressure broadening of the homogeneous optical linewidth Γ is of no importance. The pressure dependence of the velocity resolution can be important, however, if the diffractive peak of the physical velocity-change spectrum leads to a somewhat increased number of small velocity changes connected with a Doppler shift that is comparable to the homogeneous optical linewidth: Such velocity changes can affect the AM-RHS linewidths only if they lie above the velocity resolution limit, i.e., for $k\,|v-v'|>\Gamma$. As a consequence, these small velocity changes might only contribute to the values of $\gamma_{\rm VCC}$ as measured at low rare-gas pressures (small Γ) while being insignificant for the AM-RHS linewidths at large pressures (large Γ). Thus, the physically expected deviations from the simple shape of the velocity-change spectrum assumed in the calculations [see Eq. (3.24)] can explain our finding that for large pressures, reduced values for $\gamma_{\rm VCC}$ have to be used in the calculations to obtain an improved agreement of measured and calculated linewidths. Up to now, however, it is not clear why the observed discrepancies are negligible or low in the case of He and Xe while they appear to be large for Ne and Ar perturbers. Some knowledge on the shapes of the interatomic potentials and of the real collision kernels would be very helpful to illuminate this point.

Let us finally note that the numerical calculations shown in Fig. 9 demonstrate that the calculated overall pressure dependence of the AM-RHS linewidths can strongly depend on the values used for $\gamma_{\rm VCC}$. Therefore, some of the discrepancies between measured and calculated AM linewidths at large pressures might also result from the fact that in our case, $\gamma_{\rm VCC}$ was derived from only one or two data points at low rare-gas densities. However, the reduction of $\gamma_{\rm VCC}$ required to fit the AM-RHS linewidths for Ne and Ar at high pressures is too large to be explained only by unprecise measurements of the rate constant $\gamma_{\rm VCC}$.

C. Results of measurements

As has been shown, the rate constants γ_c ($\gamma_{\rm VCC}$) can be derived directly from the FM- (AM-)RHS linewidths at large (low) buffer-gas pressures. The collisional cross sections σ_c and $\sigma_{\rm VCC}$ are connected to the corresponding rate constants through the general relation

$$\gamma=N_P v_r\sigma\ , \tag{5.1}$$

where $N_P=p/(k_BT)$ denotes the perturber density, and v_r is the average relative thermal speed,

$$v_r=\left[\frac{8k_BT}{\pi}\left[\frac{1}{m_A}+\frac{1}{m_P}\right]\right]^{1/2}\ , \tag{5.2}$$

with m_A and m_P being the mass of active and perturber atoms, respectively. Table I shows the value for σ_c and $\sigma_{\rm VCC}$ that were obtained from our experimental data, listed together with the hard-sphere collisional cross sections $\sigma_h=\pi(r_A+r_P)^2$ derived from tabulated values for the atomic radii r_A and r_P.[23] We assume a relative error in σ_c of typically $\pm 10\%$, whereas the values given for $\sigma_{\rm VCC}$ are only first estimates based on the small number of data points at low rare-gas pressures. In Table I we also show the values of the Keilson-Storer parameter α that resulted in the best overall agreement of measured and calculated AM-RHS linewidths. For He, Ne, and Ar, the displayed hard-sphere values α_h give a width of the used collision kernel (2.24) which corresponds to the width of the hard-sphere collision kernal in the limit of light perturbers ($m_P\ll m_A$).[17]

An intuitive interpretation of the experimental data for σ_c, $\sigma_{\rm VCC}$, and α is possible by comparing them to the hard-sphere values σ_h and α_h: The ratio of VCC and hard-sphere collisional cross sections varies between

TABLE I. Experimentally determined values for the collision parameters. For comparison, the hard-sphere values σ_h and α_h are also displayed.

Perturber	σ_c (Å^2)	σ_{VCC} (Å^2)	σ_h (Å^2)	α	α_h
He	1.4	180	28	0.985	0.966
Ne	5.3	240	30	0.94	0.836
Ar	12	320	36	0.93	0.670
Xe	16	340	47	0.95	

$\sigma_{VCC}/\sigma_h \simeq 6$ (He) and $\sigma_{VCC}/\sigma_h \simeq 9$ (Ar). This indicates that, essentially independent of the mass of the perturber atoms, the velocity changes connected with the long-range part of the interatomic potential are in our case sufficient to remove the active atoms from optical resonance. It is consistent with this picture to obtain $\alpha > \alpha_h$, i.e, the actual average collisional velocity changes are smaller than in the hard-sphere limit; as has been mentioned above, however, the values of α given here can only serve as a rough estimate for the width of the broad part of the physical collision kernel.

We also note that the measured cross sections for depolarizing collisions, σ_c, are always smaller than σ_{VCC} by 1 to 2 orders of magnitude. This fact is not surprising since calculations predict an only weakly disturbed spherical symmetry for the electronic charge distribution of the Sm $4f^6 6s^2$ configuration at large radii due to the large effective radius of the $6s^2$ orbital.[24] As a consequence, the anisotropy of the Sm $^7F_1$ ground-state–rare-gas collision potential is negligible in its long-range part, and the ground-state Zeeman coherence is preserved during collisions with large impact parameters ("weak" collisions). In the case of He perturbers, the large difference between σ_c and the hard-sphere cross section σ_h in addition yields a low probability of collisional depolarization also for collisions with a small impact parameter ("strong" collisions). For Ne, Ar, and Xe perturbers, the considerably larger values for σ_c indicate that here strong collisions can efficiently destroy the Zeeman coherence. This fact suggests that, compared to He perturbers, the heavier rare gases show increased contributions of weak collisions in the velocity diffusion of Hertzian coherence.

VI. SUMMARY AND OUTLOOK

We have studied collision effects in a rf-laser double-resonance experiment on a Zeeman split $J=1 \rightarrow J'=0$ transition using Raman heterodyne detection of the rf-excited ground-state sublevel coherence. The well-defined velocity selectivity of AM- and FM-RHS has offered the possibility to separately analyze the signal contributions of different velocity subgroups, thus revealing the influence of sublevel coherence-preserving, velocity-changing collisions on the line shapes of the optically detected rf resonances. A novel theoretical description of the rf-optical double resonance process has been presented that phenomenologically takes into account the collisional velocity diffusion of the active atoms during their rf excitation. The predicted signal features have been demonstrated with atomic samarium vapor and rare-gas collision partners; from the comparison of calculated and measured results cross sections for both VCC and depolarizing collisions have been derived. Moreover, information on the spectrum of the velocity changes connected with alignment-preserving collisions has been obtained.

The observed discrepancies between measured and calculated RHS linewidths are probably related to the simple assumptions of the present theoretical model. A refined theoretical description that permits a more appropriate choice of the collision kernel and that takes into account the limitations in velocity resolution, should remove these discrepancies and lead to more elaborate data especially for the relevant velocity-change spectrum. It may be noted in this context that our double-resonance technique is in principle applicable to both electronic ground states and optically excited states with a high sensitivity; for the detailed study of the collisional relaxation of Zeeman sublevels, the method might therefore be an interesting alternative to the current techniques using stimulated photon echoes.[9] In contrast to photon-echo experiments, however, the velocity resolution obtainable with the measurement of rf resonance linewidths in cw experiments is strictly limited to velocity changes yielding a Doppler shift of more than the homogeneous optical linewidth.

Our discussion of the effect of velocity-changing collisions in a rf-laser double-resonance experiment also contributes to a new vista into the role of collisions in laser spectroscopy of sublevel structures: The limitation of the observation time of the active atoms due to narrow-bandwidth optical excitation and simultaneous velocity diffusion can be of importance for a variety of spectroscopic techniques that use a velocity-selective excitation and detection of either sublevel populations or sublevel coherence; one specific example is the measurement of ground-state level-crossing resonances in Doppler-broadened samples with the use of narrow-bandwidth laser excitation.[25,26] On the other hand, the collisional velocity diffusion of sublevel coherence within an optical Doppler distribution can also give rise to new phenomena. In this context, we note the recent observation of Ramsey resonances in a purely optical-optical double-resonance experiment in Sm vapor due to VCC.[27] In general, the influence of VCC on the resolution of the sublevel energy splitting in a particular experiment will depend on the experimental technique as well as on the studied atomic or molecular system. The calculation of the expected VCC effects should be possible in many cases with formalisms similar to the one displayed in this paper.

We also note that VCC may serve as a model for relaxation mechanisms found in solids.[28,29] A recent derivation, e.g., of modified optical Bloch equations for solids uses a formalism that bears a close analogy to transport equations describing the effects of collisions in atomic vapors.[29] Thus, the calculation and observation of VCC effects in a rf-laser double-resonance experiment may stimulate new relaxation and line-broadening studies in solid-state spectroscopy. As a specific example we mention Raman heterodyne studies on magnetic line-broadening processes in dilute impurity ion crystals in the limit of high rf excitation fields.[30] Moreover, the experimental technique reported here may offer new possibilities to study interline energy transfer processes arising from ion-ion interactions in solids under conditions of narrow-bandwidth laser excitation;[31] in this context the knowledge on collision effects in atomic vapors might also prove useful to model such spectral diffusion among ions in crystals.

The technique of AM and FM Raman heterodyne detection of rf-optical double resonance in gaseous samples also has a large potential beyond the study of atomic collisions. The narrow-bandwidth detection of the rf beat signal corresponding to the AM-RHS can be used for a highly sensitive, background-free measurement of weak absorptions in Doppler-broadened media or atomic beams, making this scheme a possible alternative to other sensitive techniques like magnetic rotation spectroscopy[32] or frequency modulation spectroscopy.[33]

The FM Raman heterodyne detection offers a new way for the study of small asymmetric distortions in the atomic velocity distribution resulting from, e.g., chemical and photochemical reactions, electronic collisions, or from the absorption of photons. Especially the effect of photon impact on the FM-RHS is of interest for future studies since the momentum of the driving light field here acts as an additional nonlinear mechanism in the generation of the Raman sidebands.[10]

ACKNOWLEDGMENTS

We are indebted to Professor Lange for stimulating discussions. One of us (Chr.T.) acknowledges support by the Studienstiftung des Deutschen Volkes and another (E.B.) by the Niedersächsische Graduiertenförderung. J. M. is supported by the Heisenberg Programm of the Deutsche Forschungsgemeinschaft. This work was funded by the Deutsche Forschungsgemeinschaft.

[1]See, e.g., P. R. Berman, in *New Trends in Atomic Physics,* edited by G. Grynberg and R. Stora (North-Holland, Amsterdam, 1984), Vol. 1, p. 451.

[2]See, e.g., C. Brechignac, R. Vetter, and P. R. Berman, Phys. Rev. A **17**, 1609 (1978); M. Gorlicki, A. Peuriot, and M. Dumont, J. Phys. (Paris) Lett. **41**, L275 (1980); I. Colomb, M. Gorlicki, and M. Dumont, Opt. Commun. **21**, 289 (1977); M. Pinard, C. G. Aminoff, and F. Laloe, Phys. Rev. A **19**, 2366 (1979).

[3]See, e.g., R. Kachru, T. J. Chen, S. R. Hartmann, T. W. Mossberg, and P. R. Berman, Phys. Rev. Lett. **47**, 902 (1981); R. A. Forber, L. Spinelli, J. E. Thomas, and M. S. Feld, *ibid.* **50**, 331 (1983).

[4]J. Mlynek, Chr. Tamm, E. Buhr, and N. C. Wong, Phys. Rev. Lett. **53**, 1814 (1984).

[5]See, e.g., C. Cohen-Tannoudji and A. Kastler, in *Progress in Optics* (North-Holland, Amsterdam, 1966), Vol. 5, p. 1.

[6]See, e.g., W. Happer, Rev. Mod. Phys. **44**, 169 (1972).

[7]J. Mlynek, N. C. Wong, R. G. DeVoe, E. S. Kintzer, and R. G. Brewer, Phys. Rev. Lett. **50**, 993 (1983); N. C. Wong, E. S. Kintzer, J. Mlynek, R. G. DeVoe, and R. G. Brewer, Phys. Rev. B **28**, 4993 (1983).

[8]J. L. Le Gouet and P. R. Berman, Phys. Rev. A **24**, 1831 (1981).

[9]A. G. Yodh, J. Golub, and T. W. Mossberg, Phys. Rev. A **32**, 844 (1985); J. C. Keller and J. L. Le Gouet, *ibid.* **32**, 1624 (1985).

[10]Chr. Tamm, R. Grimm, and J. Mlynek (unpublished); R. Grimm, Diploma thesis, Hannover University, 1986 (unpublished).

[11]A. R. Edmonds, *Angular Momentum in Quantum Mechanics* (Princeton University Press, Princeton, 1960).

[12]P. R. Berman, in *Advances in Atomic and Molecular Physics* (Academic, New York, 1977), Vol. 13, p. 57, and references therein.

[13]Throughout this paper, sublevel coherence will also be termed Hertzian coherence following a notation by A. Kastler [A. Kastler, Science **158**, 214 (1976)].

[14]See, e.g., E. Hecht and A. Zajac, *Optics* (Addison-Wesley, Reading, Mass., 1974), p. 269.

[15]P. R. Berman, T. W. Mossberg, and S. R. Hartmann, Phys. Rev. A **25**, 2550 (1982).

[16]J. Keilson and A. E. Storer, Q. Appl. Math. **10**, 243 (1952).

[17]J. L. Le Gouet, J. Phys. B **11**, 3001 (1978).

[18]Chr. Tamm. Ph. D. thesis, Hannover University, 1986 (unpublished).

[19]*Handbook of Mathematical Functions,* Natl. Bur. Stand. Appl. Math. Ser. No. 55, edited by M. Abramowitz and I. A. Stegun (U.S. GPO, Washington, D.C., 1972), p. 297.

[20]A. Carlier, J. Blaise, and M. G. Schweighofer, J. Phys. (Paris) **29**, 729 (1968).

[21]M. G. Ingram, D. C. Hess, Jr., and R. J. Hayden, Phys. Rev. **73**, 180 (1948).

[22]P. Hannaford and R. M. Lowe, J. Phys. B **18**, 2365 (1985).

[23]C. W. Allen, *Astrophysical Quantities,* 2nd ed. (University of London Press, London, 1963), p. 45; the radius of Sm atoms was derived from the lattice constant of solid Sm, C. Kittel, *Introduction to Solid State Physics,* 5th ed. (Wiley, New York, 1976).

[24]W. Lange (private communication).

[25]K. H. Drake, J. Mlynek, and W. Lange, Verh. Dtsch. Phys. Ges. **20**, 1038 (1985); K. H. Drake, Ph.D. thesis, Hannover University, 1986 (unpublished).

[26]R. J. McLean, D. S. Gough, P. Hannaford, in *Laser Spectroscopy VII,* edited by T. W. Hänsch and Y. R. Shen (Springer-Verlag, Heidelberg, 1985), p. 220.

[27]J. Mlynek, E. Buhr, and Chr. Tamm, in *Methods in Laser Spectroscopy,* edited by Y. Prior (Plenum, New York, 1986), p. 175; E. Buhr and J. Mlynek, Phys. Rev. Lett. (to be published).

[28]R. G. Yodh, J. Golub, N. W. Carlson, and T. W. Mossberg, Phys. Rev. Lett. **53**, 659 (1984).

[29]P. R. Berman and R. G Brewer, Phys. Rev. A **32**, 2784 (1985).
[30]A. Schenzle, M. Mitsunaga, R. G. DeVoe, and R. G. Brewer, Phys. Rev. A **30**, 325 (1984); M. Mitsunaga, E. S. Kintzer, J. Mlynek, and R. G. Brewer (unpublished).
[31]W. M. Yen and P. M. Selzer, in *Laser Spectroscopy of Solids*, edited by W. M. Yen and P. M. Selzer (Springer-Verlag, Heidelberg, 1981), p. 165.
[32]G. Litfin, C. R. Pollock, R. F. Curl, Jr., and F. K. Tittel, J. Chem. Phys. **72**, 6602 (1980).
[33]G. C. Bjorklund, Opt. Lett. **5**, 15 (1980).